Physics of Fluids

RESEARCH ARTICLE | APRIL 10 2024

Instability mechanisms of symmetry breaking in the wakes of two anti-phase pitching foils at zero free-stream velocity

Zhiyu Zhang ; Xing Zhang

Physics of Fluids 36, 043610 (2024)
https://doi.org/10.1063/5.0196194

Physics of Fluids ARTICLE pubs.aip.org/aip/pof

Instability mechanisms of symmetry breaking in the wakes of two anti-phase pitching foils at zero free-stream velocity

Cite as: Phys. Fluids **36**, 043610 (2024); doi: 10.1063/5.0196194
Submitted: 5 January 2024 · Accepted: 19 March 2024 ·
Published Online: 10 April 2024

Zhiyu Zhang[1,2] and Xing Zhang[1,2,a)]

AFFILIATIONS

[1]The State Key Laboratory of Nonlinear Mechanics, Institute of Mechanics, Chinese Academy of Sciences, Beijing 100190, China
[2]School of Engineering Science, University of Chinese Academy of Sciences, Beijing 100049, China

[a)]Author to whom correspondence should be addressed: zhangx@lnm.imech.ac.cn

ABSTRACT

In the present study, we investigate into the symmetry-breaking phenomenon in the wakes produced by two anti-phase pitching foils at zero free-stream velocity. Numerical simulations are performed in a gap ratio range of $0.6 \leq g \leq 2.0$ and a Reynolds number range of $70 \leq Re \leq 200$. Six regions are identified in the plane (g, Re), based on distinct symmetry-breaking (or symmetry-preserving) behaviors of the wakes. Floquet stability analysis and dynamic mode decomposition are performed on some selected cases. By means of modal analysis, the behaviors of wakes in different regions are rationalized and the instability mechanisms of symmetry breaking in the unstable regions are unveiled. In addition, the influence of symmetry-breaking instability on propulsive performance is also discussed.

I. INTRODUCTION

Symmetry-related problems are widely encountered in fluid mechanics. Here, we can distinguish between two types of symmetry: spatial (reflection or rotation) symmetry and spatiotemporal symmetry (i.e., reflection symmetry after half a period). Symmetry breaking in the wake is one phenomenon that is often observed in flows around stationary and moving objects.

It is well known that such phenomenon occurs in flow past a circular cylinder, which is one classical problem of fluid mechanics. Above a critical Reynolds number, the reflection symmetry of the steady wake featured by a pair of separation bubbles is broken. The wake eventually transits into a periodic vortex street with spatiotemporal symmetry. It has been revealed by using linear stability analysis that the transition from steady to periodic state can be described via a Hopf bifurcation.[1,2] In flow past two side-by-side cylinders, six different wake patterns, namely, steady symmetric, steady asymmetric, single bluff-body, in-phase synchronized, anti-phase synchronized, and flip-flopping, were identified at different values of gap distance and Reynolds number.[3] The results of global stability analysis indicated that spatial reflection symmetry or spatiotemporal symmetry was broken when a steady anti-symmetric mode or a harmonic mode became unstable.[4–6]

The wake of an oscillating cylinder in quiescent fluid possesses both reflection symmetry and spatiotemporal symmetry. It was discovered in experiments and simulations that one type of symmetry (or both) can be broken when the Keulegan–Carpenter (KC) number is high enough.[7–10] By using Floquet stability analysis, two types of instability, namely, synchronous (S) and quasiperiodic (QP), were identified at different ranges of Stokes number.[11–13] Such study was then extended to oscillating elliptic cylinders with different aspect ratios. The influence of aspect ratio on the location of neutral stability curve in a parametric space spanned by KC and Stokes numbers was investigated.[14]

The symmetry property of wakes generated by flapping foils also attracted the attention of researchers. This is because it is closely related to the propulsive performance of flapping-powered swimming and flying. Here, we briefly review the studies on wakes generated by a single flapping foil and two side-by-side pitching foils. The flapping foils can be subjected to free-swimming (self-propelled) condition where its speed is the result of interaction with the fluid. Or alternatively, the flapping foils can be tethered in a flow with prescribed velocity. This is equivalent to the situation in which the flapping foils are towed at a given speed. As an extreme case of the latter type, the velocity of incoming flow can be reduced to zero. This corresponds to the situation in which a swimmer is constrained to remain at a fixed position in water or a flyer hovers in air under the influence of gravity.

The development of deflected (asymmetric) wakes behind a single flapping foil is a phenomenon of spatiotemporal symmetry breaking,

which has been reported both in experiments and in simulations. By using Floquet analysis, this phenomenon was explained by the fact that one synchronous anti-symmetric mode became unstable at a critical flapping frequency.[15] For cases with a nonzero free-stream velocity, the wake inclination (either leftward or rightward) was found to be determined by the initial condition.[16,17] In some recent papers, it was also found that further increase in flapping amplitude can result in the transition of flow-field from periodicity to chaos.[18–20] At zero free-stream velocity, however, the wake inclination was found to vary continually with time. This wake meandering was found to be random and independent of the initial condition.[21] The influence of passive flexibility on wake transition was also addressed in some studies.[22–25]

The model of two side-by-side pitching foils has several sources of biological inspirations, such as miniature fish schools, swimming jellyfish, and insect wings with a clap-and-fling motion.[26–29] The propulsive performance of such model under tethered condition in a steady free-stream flow has been extensively studied at different values of Strouhal number, phase difference, flapping amplitude, and separation distance.[30–35] Three distinct wake patterns, namely, separated wake, merged wake, and transitional-merged wake, were identified.[35] In the scenario of anti-phase pitching, it was found that reflection symmetry of the wake was broken at high Strouhal numbers.[31,32] The formation of a deflected jet was reported in a study on two side-by-side pitching foils in a quiescent fluid.[36] In a recent study on the hovering stability of such flapper under gravitational force,[37,38] it was found that although wake symmetry can be preserved for as long as 20–30 flapping periods, symmetry breaking was eventually triggered. The hovering of a flexible Λ-shaped flyer in a vertically oscillating flow under free-flying condition was also investigated.[39] It was affirmed that at certain ranges of oscillating frequency and amplitude, wake symmetry breaking can be suppressed by the passive pitching of the foils. In all the studies above, the occurrence of wake symmetry breaking was found to be detrimental to either efficiency of thrust generation or postural stability.

It is worth noting that there exists an analogy between a pair of anti-phase pitching foils with a single foil operating near the ground.[40–44] Obviously, these two configurations bear some resemblance in wake structure and thrust enhancement (in comparison with a single foil operating in open space). However, one needs to be cautious that such analogy is only rigorous in inviscid sense. Under the inviscid-flow assumption, by invoking the method of images, ground effect can be represented as a second foil which undergoes a pitching motion out-of-phase with the original one. Furthermore, such analogy also implies that reflection symmetry of the wake is always preserved.

In some existing studies on anti-phase pitching foils, the wake evolution (including symmetry breaking process) was detailed. In other studies, possible conditions for triggering wake symmetry breaking have been summarized, e.g., local accumulation of vorticity and strong interaction between two parallel wakes. However, the instability mechanisms related to symmetry breaking are still not fully understood. In this paper, we investigate into this subject by using an approach which combines direct numerical simulation (DNS), Floquet stability analysis, and dynamic mode decomposition (DMD). The results of this study provide some new insight into the phenomenon of wake symmetry breaking. The novel contribution of the present work is that it is the first attempt to study the instability mechanisms in the interaction of two parallel *thrust-producing* wakes using modal analysis methods. To the best of our knowledge, in the past such methods have only been applied to study the interaction of two parallel *drag-producing* wakes.

II. PROBLEM DESCRIPTION AND GOVERNING EQUATIONS

A. Computational model

In this study, we consider one pair of rigid thin foils which undergoes anti-phase pitching motion. Unlike the self-propelled system considered in the past study,[37] in the present study the dual-foil system is tethered in the fluid. A schematic view of the physical model is presented in Fig. 1. The kinematics of the flapping foils is described as

$$\theta_{1,2}(t) = \pm[\theta_0 + A_\theta \cos(2\pi t)], \tag{1}$$

where θ_1 and θ_2 are the instantaneous pitching angles, θ_0 is the equilibrium angle, A_θ is the flapping amplitude, and t is the dimensionless time which is related to the dimensional time t^* by $t = t^* f$ (where f is the flapping frequency). The dimensionless flapping period T thus equals unity. Obviously, the configuration of the computational model (in terms of geometry and kinematics) is symmetric with respect to the centerline ($x = 0$).

We consider the spontaneous transition of the wake from a symmetric state to an asymmetric state as the result of flow instability. The flow fields before occurrence of symmetry breaking possess the symmetric property defined as

$$\begin{aligned} u_x(x,y,t) &= -u_x(-x,y,t), \\ u_y(x,y,t) &= u_y(-x,y,t), \\ \omega_z(x,y,t) &= -\omega_z(-x,y,t), \end{aligned} \tag{2}$$

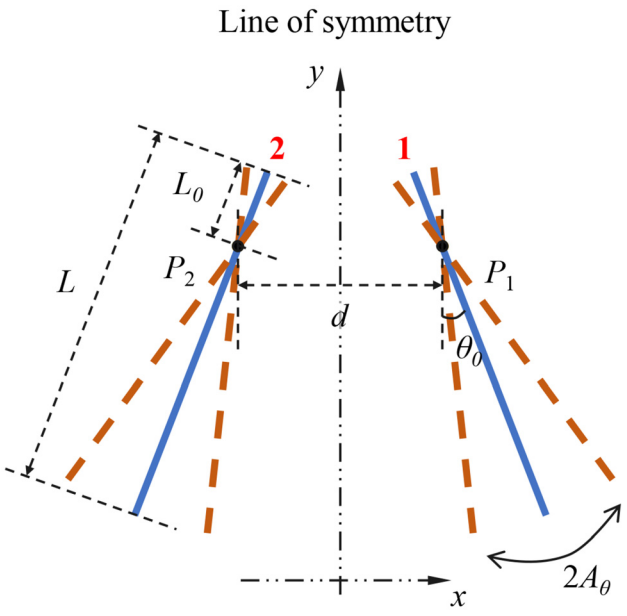

FIG. 1. Schematic diagram of the physical model. d, L, and L_0 denote the distance between the two pivot points, the chord length, and the distance from the pivot point to the leading end, respectively; θ_0 and A_θ denote the equilibrium angle and the flapping amplitude; and P_1 and P_2 denote the pivot points of the two foils.

where u_x and u_y denote the horizontal and vertical components of velocity, and ω_z denotes the vorticity component in the direction perpendicular to x–y plane. In contrast, the flow fields of some unstable modes in modal analysis to be discussed later possess the anti-symmetric property defined as

$$\begin{aligned} u_x(x,y,t) &= u_x(-x,y,t),\\ u_y(x,y,t) &= -u_y(-x,y,t),\\ \omega_z(x,y,t) &= \omega_z(-x,y,t). \end{aligned} \tag{3}$$

B. Navier–Stokes equations

The flow around the pitching foils is assumed to be laminar and governed by incompressible Navier–Stokes equations, which can be written in a dimensionless form as

$$\frac{\partial \boldsymbol{u}}{\partial t} + (\boldsymbol{u}\cdot\nabla)\boldsymbol{u} = -\nabla p + \frac{1}{\mathrm{Re}}\nabla^2\boldsymbol{u} + \boldsymbol{f}, \tag{4a}$$

$$\nabla\cdot\boldsymbol{u} = 0, \tag{4b}$$

where $\boldsymbol{u}$ is the velocity vector and p is the pressure. $\boldsymbol{f}$ is the momentum source term which represents the interaction between the fluid and the foils. In the immersed boundary method, which is used to solve (4), $\boldsymbol{f}$ is implicitly determined by enforcing the no-slip condition on the surfaces of the foils.

The reference length, time, and velocity used in the nondimensionalization are L (chord length), $1/f$, and Lf, respectively. The Reynolds number Re is defined as $Re = L^2 f/\nu$, where ν is the kinematic viscosity of the fluid. Please note that this Reynolds number is based on the flapping velocity, and is different from the commonly used one which is based on the free-stream velocity. For free-swimming or forward-flying animals, the free-stream Reynolds number and flapping-based Reynolds number are usually of the same order in magnitude.

Other dimensionless control parameters of the systems are: the dimensionless distance from the pivot point to the leading end $\hat{L} = L_0/L$, the gap ratio (i.e., dimensionless gap distance between the two pivot points) $g = d/L$, the equilibrium angle θ_0, and the flapping amplitude A_θ.

C. Linearized equations for the perturbation

The solution of the Navier–Stokes equations can be decomposed into a base flow and a perturbation as

$$\boldsymbol{u} = \boldsymbol{U} + \boldsymbol{u}', \quad p = P + p', \quad \boldsymbol{f} = \boldsymbol{F} + \boldsymbol{f}', \tag{5}$$

where $\boldsymbol{U}$, P, and $\boldsymbol{F}$ denote the velocity, pressure, and forcing of a periodic base flow, while $\boldsymbol{u}'$, p', and $\boldsymbol{f}'$ denote the small perturbations in velocity, pressure, and forcing, respectively. The linearized equations for the perturbation can be obtained by substituting (5) into (4), subtracting from them the base flow, and dropping the nonlinear term of velocity perturbation. The linearized equations for the perturbation are

$$\frac{\partial \boldsymbol{u}'}{\partial t} + (\boldsymbol{U}\cdot\nabla)\boldsymbol{u}' + (\boldsymbol{u}'\cdot\nabla)\boldsymbol{U} = -\nabla p' + \frac{1}{\mathrm{Re}}\nabla^2\boldsymbol{u}' + \boldsymbol{f}', \tag{6a}$$

$$\nabla\cdot\boldsymbol{u}' = 0. \tag{6b}$$

Similar to its counterpart $\boldsymbol{f}$ in (4a), the forcing term $\boldsymbol{f}'$ in (6a) is implicitly determined in the immersed boundary method by enforcing the no-slip condition (i.e., $\boldsymbol{u}' = 0$) on the surfaces of the foils.

D. Floquet stability analysis

Equation (6) can be written is a more concise form as

$$\frac{\partial \boldsymbol{u}'}{\partial t} = \mathscr{A}(\boldsymbol{U}(t))\boldsymbol{u}', \tag{7}$$

where $\mathscr{A}$ is a linear operator and the base-flow velocity $\boldsymbol{U}$ is T-periodic. It should be noted that in addition to the convection and diffusion terms, the projection operation (for obtaining a divergence-free velocity perturbation) is also lumped into operator $\mathscr{A}$.

According to the Floquet theory,[45] the velocity perturbation can be expressed as the summation of components by

$$\boldsymbol{u}'(\boldsymbol{x},t) = \sum_k \hat{\boldsymbol{u}}_k(\boldsymbol{x},t)e^{\lambda_k t}, \tag{8}$$

where $\hat{\boldsymbol{u}}_k$ are the T-periodic Floquet eigenfunctions and λ_k are the Floquet exponents. The Floquet multipliers defined as $\mu_k = e^{\lambda_k T}$ signify the growth or decay of the Floquet modes over one period T. The Floquet multipliers can be either real numbers or complex-conjugate pairs. Instability occurs if the modulus of one Floquet multiplier is larger than unity, or equivalently, if the real part of one Floquet exponent is positive.

E. Dynamic mode decomposition

Dynamic mode decomposition (DMD) is a data-based method to decompose time-resolved data into modes. Each mode possesses a single characteristic frequency of oscillation and a growth rate. The DMD modes are obtained through the eigen-decomposition of a best-fit linear operator that approximates the evolution of dynamic system state.

In this paper, the inputs of DMD analysis are snapshots of flow-field data (i.e., x and y velocity components), which are arranged as matrices $\mathbf{X}$ and $\mathbf{Y}$, such that

$$\begin{aligned} \mathbf{X} &= \{\mathbf{x}(t_1), \quad \mathbf{x}(t_2), \quad \dots \quad, \mathbf{x}(t_m)\} \in \mathbb{R}^{n\times m},\\ \mathbf{Y} &= \{\mathbf{x}(t_2), \quad \mathbf{x}(t_3), \quad \dots \quad, \mathbf{x}(t_{m+1})\} \in \mathbb{R}^{n\times m}. \end{aligned} \tag{9}$$

Here, $\mathbf{x}(t_i)$ are the vectors for storing flow-field data of different snapshots. The data are collected at time instants t_i, with a uniform sampling increment between snapshot pairs. n is twice the number of mesh points and m is the number of snapshots.

In DMD analysis, a linear relationship between the two aforementioned matrices is assumed such that

$$\mathbf{Y} = \tilde{\mathbf{A}}\mathbf{X}. \tag{10}$$

The eigenvalues and eigenvectors of $\tilde{\mathbf{A}}$ are defined as DMD eigenvalues and DMD modes.

III. NUMERICAL METHODS

A. Solutions of Navier–Stokes equations and linearized equations

The direct-forcing immersed boundary method based on discrete streamfunction formulation[46,47] is used to solve the Navier–Stokes equations and the linearized equations. The algebraic multigrid method is used to solve the linear systems arising from numerical discretization. The code is parallelized by using the message passing interface (MPI) protocol.[48] Validations of the flow solver have been

performed in some previous studies by simulating flows over stationary and moving objects.[46,47]

B. Solutions of eigenvalue problems

To compute the Floquet modes and multipliers, a method similar to that introduced by Tuckerman and Barkley[49] is used. First, the evolution equation for the discretized velocity perturbation over one period can be expressed as

$$\boldsymbol{u}_h'(t_0+T) = \mathsf{A}\boldsymbol{u}_h'(t_0), \tag{11}$$

where $\boldsymbol{u}_h'$ denotes the vector of the spatially discretized velocity perturbation (with the size of $2 \times M$ in which M is the number of grid points). The matrix A is the propagator over one period (also known as the linearized Poincaré map). The operation of A on the velocity perturbation is performed by integrating (7) over one period T.

The eigenvalues of A are the Floquet multipliers μ_k, and the eigenvectors of A are the Floquet eigenfunctions $\hat{\boldsymbol{u}}_k$ for an arbitrary initial time t_0. A Krylov subspace iteration with the modified Gram–Schmidt algorithm for the orthogonalization procedure is used to obtain the eigenvalues and eigenvectors of A.[50]

In this study, DMD analysis is performed by using a Python package, PyDMD.[51] An overview of the DMD algorithm implemented in this package is provided here. In the algorithms of DMD, since the dimension of $\tilde{\mathbf{A}}$ scales with the number of mesh points, it is not efficient to compute $\tilde{\mathbf{A}}$ explicitly. Instead, the eigenvalues of a low-dimensional matrix are used to approximate those of the original one.[52]

First, the singular value decomposition (SVD) of matrix $\mathbf{X}$ is performed,

$$\mathbf{X} = \mathbf{U}\boldsymbol{\Sigma}\mathbf{V}^*, \tag{12}$$

where $\mathbf{U} = [u_1, u_2, \ldots, u_n] \in \mathbb{C}^{n\times n}$ and $\mathbf{V} = [v_1, v_2, \ldots, v_m] \in \mathbb{C}^{m\times m}$ are the unitary matrices and $\boldsymbol{\Sigma} \in \mathbb{R}^{n\times m}$ is a diagonal matrix with $\sigma_1 \geqslant \sigma_2 \geqslant \cdots \geqslant \sigma_p \geqslant 0$ along its diagonal, where $p = \min(n, m)$, "$*$" denotes the conjugate transpose.

The SVD is then truncated by only considering the first r singular values and singular vectors and matrix $\tilde{\mathbf{A}}$ can be approximated as

$$\hat{\mathbf{A}} = \mathbf{U}_r^T\tilde{\mathbf{A}}\mathbf{U}_r = \mathbf{U}_r^T\mathbf{Y}\mathbf{V}_r\boldsymbol{\Sigma}_r^{-1} \in \mathbb{R}^{r\times r}, \tag{13}$$

where $\mathbf{U}_r = [u_1, u_2, \ldots, u_r] \in \mathbb{C}^{n\times r}$, $\mathbf{V}_r = [v_1, v_2, \ldots, v_r] \in \mathbb{C}^{m\times r}$ are unitary matrices and $\boldsymbol{\Sigma}_r \in \mathbb{R}^{r\times r}$, "$T$" denotes the transpose.

The eigenvalues $\hat{\mu}_j$ and eigenvectors $\hat{\mathbf{v}}_j$ of $\hat{\mathbf{A}}$ can then be found, with $\hat{\mathbf{A}}\hat{\mathbf{v}}_j = \hat{\mu}_j\hat{\mathbf{v}}_j$. The eigen-decomposition of $\hat{\mathbf{A}}$ in matrix form becomes $\hat{\mathbf{A}}\hat{\mathbf{V}} = \hat{\mathbf{V}}\mathbf{M}$, where $\hat{\mathbf{V}} = [\hat{\mathbf{v}}_1, \hat{\mathbf{v}}_2, \ldots, \hat{\mathbf{v}}_r] \in \mathbb{C}^{r\times r}$, and $\mathbf{M} \in \mathbb{C}^{r\times r}$ is a diagonal matrix with $\hat{\mu}_j$ along its diagonal.

The eigen-decomposition of $\tilde{\mathbf{A}}$ can then be expressed as

$$\begin{aligned} \tilde{\mathbf{A}}\mathbf{U}_r\hat{\mathbf{V}} &= \mathbf{M}\mathbf{U}_r\hat{\mathbf{V}}, \\ \tilde{\mathbf{A}}\boldsymbol{\Phi} &= \boldsymbol{\Phi}\mathbf{M}, \end{aligned} \tag{14}$$

where $\boldsymbol{\Phi} = \mathbf{Y}\mathbf{V}_r\boldsymbol{\Sigma}_r^{-1}\hat{\mathbf{V}} \in \mathbb{C}^{\mathbf{n}\times\mathbf{r}}$. The DMD amplitude, which determines the relative contribution of each DMD mode, is defined as $\mathbf{a} = \boldsymbol{\Phi}^*\mathbf{x}(t_1) \in \mathbb{C}^{r\times 1}$. In the subsequent text, the modulus of each component of $\mathbf{a}$ is referred to as "amplitude of DMD mode."

The jth DMD mode is computed by $\mathbf{v}_j = \mathbf{U}\hat{\mathbf{v}}_j$. The eigenvalues in another form, namely, $\hat{\lambda}_j$, are defined as

$$\hat{\lambda}_j = \log(\hat{\mu}_j)/(2\pi\Delta t_s), \tag{15}$$

where Δt_s denotes the sampling increments between snapshot pairs. $\mathrm{Im}(\hat{\lambda}_j)$ and $\mathrm{Re}(\hat{\lambda}_j)$ are the oscillation frequency and growth/decay rate of the DMD modes, respectively.

C. Code validation

The in-house flow solver and linear stability code are validated by performing direct numerical simulation and Floquet stability analysis on two-dimensional flows produced by an oscillating circular cylinder. The curve of neutral stability in the parameter space spanned by KC number and Stokes number is determined by direct numerical simulation and the result is compared with those from other Refs. 8 and 11. The moduli of Floquet multipliers for some cases are also compared with the reference solutions.[12] It is confirmed that both the stability boundary and the moduli of Floquet multipliers are in excellent agreement with those from the references. The DMD code is validated by applying it to transient cylinder-wake data and is benchmarked against the DMD results from Ref. 53. More detailed information on the code validation tests is provided in Appendix A.

IV. COMPUTATIONAL DETAILS

A. Physical parameters and performance metrics

The parameter range considered in the simulations is largely comparable with the reference solutions.[37] Here, we only consider the scenario of zero free-stream velocity, which corresponds to the hovering state of a self-propelled flyer. Three parameters for the geometry and kinematics of the dual-foil system are fixed, i.e., $\hat{L} = 0.2$, $\theta_0 = 0$, $A_\theta = \pi/12$.

The flapping Reynolds number and gap ratio are allowed to vary in the ranges of 70–200 and 0.6–2.0, respectively. The primary reason for choosing such range of Reynolds number is that we would like to align it with that of Ref. 37, where symmetry breaking in the wake of a dual-pitching-foil system was observed. Such Reynolds number range also coincides with that in locomotion of small insects and small jellyfish.[54–56] The influences of these two parameters on the symmetry-breaking (or symmetry-preserving) behaviors of the system are the focus of the present study.

The lateral-force coefficient C_{f_x} and thrust coefficient C_{f_y} are the two metrics for quantifying propulsive performance. The definitions of the two coefficients are

$$\begin{aligned} C_{f_x} &= \frac{F_x}{0.5(U_{te})^2 L}, \\ C_{f_y} &= \frac{F_y}{0.5(U_{te})^2 L}. \end{aligned} \tag{16}$$

Here, F_x and F_y are the horizontal and vertical components of the resultant force exerted on the dual-foil system. U_{te} is the maximum trailing-edge velocity (i.e., $U_{te} = 2\pi f \times 0.8L$). Please note that the *dimensionless* force components computed by solving (4) is based on the reference velocity fL. Thus, a factor $\frac{2}{(1.6\pi)^2}$ should be multiplied to convert them into the coefficients defined in (16). In the subsequent text, we also use $\bar{C}_{fx}$ and $\bar{C}_{fy}$ to denote time-averaged force coefficients.

B. Numerical settings

A rectangular computational domain of $[-20L, 20L] \times [-24L, 26L]$ is used for solving Navier–Stokes equations (4). The two flapping foils are arranged symmetrically about the line of symmetry ($x=0$), with the pivot points located at $[\pm d/2, 6L]$. A multi-block Cartesian mesh is used in the simulations (see Fig. 2). The grids with a uniform width of $0.005L$ are deployed in the vicinity of the flapping foils. The grid width near the outer boundaries is enlarged to $0.08L$. It is worth noting that the positions of grid points are also perfectly symmetric with respect to the line of symmetry. The same computational domain and mesh are also used for solving the linearized equations (6). The time step size used in the simulations is $0.001T$. This time step size can guarantee that the temporal resolution is sufficient and the maximal Courant–Friedrichs–Lewy (CFL) number is less than unity. In solving the linear systems arising from numerical discretization, the iterative solver stops when the residual magnitude becomes less than 10^{-5}.

The boundary conditions for solving Navier–Stokes equations (4) are as follows. The no-slip boundary condition on the surfaces of the flapping foils is enforced by using the immersed boundary method. The constant pressure outlet boundary condition is prescribed on the top and the bottom boundaries. The slip-wall boundary condition is imposed on the left and the right boundaries. More specifically, the normal velocity component and the normal gradient of the tangential velocity component are set to zero. The direct numerical simulation is initiated with a "no-flow" condition. The initial velocities of the entire flow field and the two foils are set to zero. The two foils start from the positions with either maximum or minimum pitching angles (i.e., $\pm[\theta_0 + A_\theta]$ or $\pm[\theta_0 - A_\theta]$). For some cases, the two different ways of starting (i.e., inward or outward) may have a great influence on the time course of wake evolution.

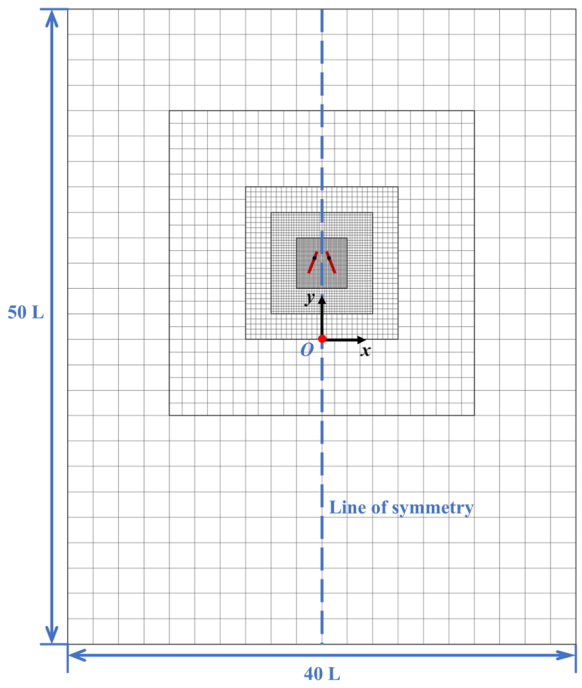

FIG. 2. Schematic diagram of the computational domain and the multi-block Cartesian mesh used in the simulations.

A periodic base flow is needed in solving the linearized equations. The base flow is obtained by solving Navier–Stokes equations (4) on the right half of the computational domain shown in Fig. 2, while imposing a slip-wall (i.e., symmetric) boundary condition on the line of symmetry. The boundary conditions on the (single) flapping foil and on the top, right, and bottom boundaries are the same as those for solving Navier–Stokes equations on the entire domain. A no-flow condition is also used as the initial condition. Similar to the dual-foil system, the way of starting the flapping motion may have a significant impact on the time course of wake evolution (and also the final state of the base flow) in some cases. The unsteady Navier–Stokes equations (on half of the computational domain) are integrated in time until periodicity is fully established. The base flow solution for the entire computational domain is obtained by mirroring the solution on the right half to the other half. This base flow solution is then reconstructed and represented as a Fourier series with 32 Fourier modes (corresponding to 64 time points over one period T) for later use in solving the linearized equations. A further increase in the number of Fourier modes is found to have an insignificant influence on the result.

In solving the linearized perturbation equations, the homogeneous boundary condition for the velocity perturbation is imposed on all outer boundaries and the surfaces of the flapping foils. In solving the eigenvalue problem by using a Krylov subspace iterative solver, the final Hessenberg matrix is not affected by the initial velocity perturbation. Here, the field of initial velocity perturbation is generated by using random numbers between 0 and 0.001 as the initial discrete streamfunction for the entire computational domain.

Tests have been conducted to ensure that the results of direct numerical simulation and linear stability analysis are (almost) independent of the grid width, time step size, and domain size. The detailed information on such tests is provided in Appendix B.

V. RESULTS AND DISCUSSION

A. Classification of wake patterns

From the DNS results, it appears that a periodic state with reflection symmetry can be reached after a transient phase which usually lasts 2–3 flapping periods after starting. In some cases, such periodic state is the ultimate state of the system and symmetry breaking is never triggered. However, in other cases, such periodic state is only a temporary state which may persist over 30–40 flapping periods. After that, the symmetry-breaking instability sets in and the ultimate state of the wake exhibits left-right asymmetry.

Six distinct wake patterns are identified in the parameter range of this study, based on the ultimate state of the system. The classification of wake patterns is summarized in the phase diagram (g, Re) shown in Fig. 3. It is seen that wake symmetry can be preserved in the region which lies below a neutral curve of stability (i.e., region I). Above the neutral curve, the parameter space can be partitioned into five regions (i.e., regions II–VI) corresponding to distinct wake instability patterns. For cases in regions II, IV, VI, and V, observed symmetry breaking signifies the incipient stage of wake transition. For cases in region III, symmetry breaking is only observed *after* the occurrence of period-doubling instability in which wake symmetry is still preserved. The symmetry-preserving (or symmetry-breaking) behaviors in the six regions aforementioned are detailed below.

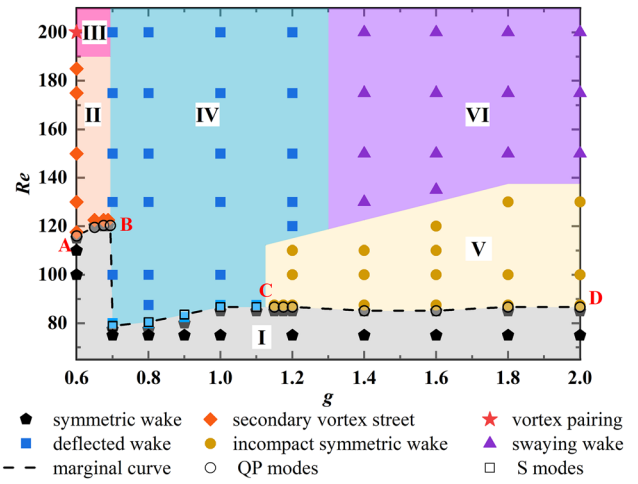

FIG. 3. The map of wake pattern classification in the two-dimensional space of (g, Re). Different colors represent sub-zones (I–VI) with distinct symmetry-breaking/preserving behaviors of the wake. The open symbols represent the critical points determined by linear stability analysis. (The coordinates of these points are obtained by interpolation such that the modulus of Floquet multiplier $|\mu| \approx 1$.) The black dashed line $A - B - C - D$ denotes the neutral stability curve, which is determined by connecting the critical points.

1. Symmetry-preserving wake pattern

The symmetric wakes for cases with different gap ratios in region I are demonstrated in Fig. 4. The profiles of vertical velocity component in the near wake are also shown. The velocity profiles shown here indicate that significant thrust is produced in all cases. It is seen that at a very small gap ratio, two vortices are trapped in between the two foils as a result of strong interaction between two vortex streets. A spike-like velocity profile which resembles that for a single jet flow is observed. As gap ratio increases, the interaction between two vortex streets is weakened. The velocity profile resembles two separate jet-flow profiles, which merge at the centerline.

2. Symmetry-breaking behaviors at small gap ratios

In region II of the diagram (with a small gap ratio and an intermediate Reynolds number), the wake pattern is featured by the formation of a secondary vortex street after the symmetry-breaking instability sets in (see Fig. 5). This secondary vortex street possesses a much larger wavelength [as indicated by λ_s in Fig. 5(d)] than that of the primary ones emanating from the trailing ends [as indicated by λ in Fig. 5(a)]. The formation of a secondary vortex street in the far wake was also observed in flow over a circular cylinder.[57–63] Despite the similarity in these two scenarios, there exists a marked difference between them. The secondary vortex street observed here is of thrust-

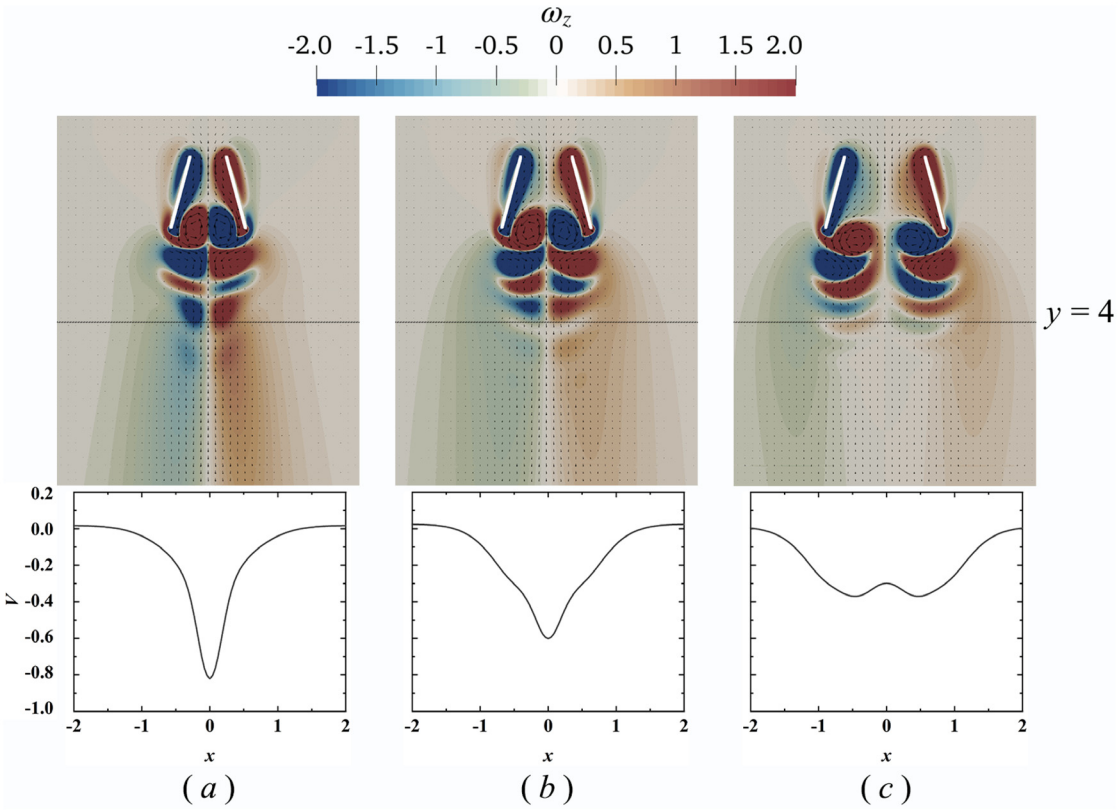

FIG. 4. Vorticity fields and velocity vectors of three cases with symmetric wake pattern (cases located in region I of Fig. 3): (a) ($g = 0.6$, $Re = 75$); (b) ($g = 0.8$, $Re = 75$); and (c) ($g = 1.2$, $Re = 75$). The two foils are located at $\pm[\theta_0 + A_\theta]$, $t = 100T$. The profiles of vertical velocity component at $y = 4.0$ for the three cases are also shown.

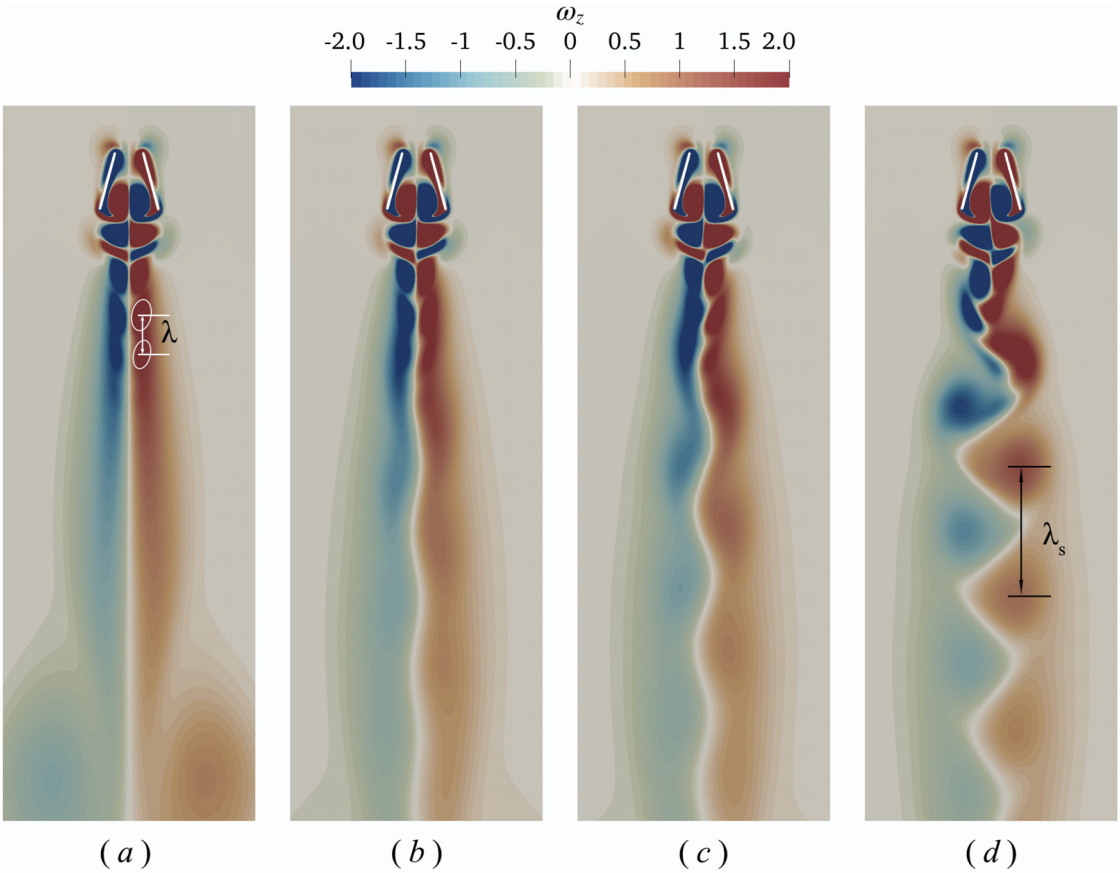

FIG. 5. Vorticity fields at various time instants in the wake evolution of ($g = 0.6$, $Re = 150$) (a case located in region II of Fig. 3): (a) $t = 40T$; (b) $t = 70T$; (c) $t = 80T$; and (d) $t = 90T$. λ denotes the wavelength of the primary vortex street.

producing (reverse Kármán) type, whereas the one in the wake of a circular cylinder is of drag-producing (Kármán) type.

In region III of the phase diagram (with a small gap ratio and a high Reynolds number), the symmetry-breaking behavior of the wake is featured by the formation of a secondary vortex street accompanied by vortex-pairing and vortex-merging (see Fig. 6). Similar to the cases in region II, the secondary vortex street possesses a much larger wavelength than that of the primary ones. In addition to this, the vortex pairing (merging) phenomenon appears repeatedly in the time course of wake evolution. First, after the transient phase, a temporarily symmetric wake is established [see Fig. 6(a)]. Intriguingly, at downstream positions of this figure, the vortex streets possess a wavelength which is roughly twice of the cases in region II. This suggests that the wake has already undergone a vortex-pairing process soon after initial starting. Second, the formation of the secondary vortex street in the far wake is induced by another vortex-pairing process [see Figs. 6(b) and 6(c)]. Third, the secondary vortex street eventually breaks up as a result of vortex merging, and superlarge vortex structures emerge in the far wake after long-term evolution [see Figs. 6(d) and 6(e)]. The vortex-pairing (or vortex-merging) phenomenon observed here shows some similarity with that observed in the laminar jet with a single-frequency inflow forcing.[64]

3. Symmetry-breaking behaviors at intermediate gap ratios

In region IV of the diagram (which lies above the neutral curve with an intermediate gap ratio), a deflected wake is observed (see Fig. 7). This asymmetric wake pattern can be easily distinguished from the ones shown in Figs. 5 and 6. Here, vortex shedding is always synchronized with the driving (flapping) motion, even after the symmetry-breaking instability sets in. In the far wake, no large-scale flow structure similar to the secondary vortex streets shown in Figs. 5 and 6 is observed. The inclination of the deflected wake (leftward or rightward) is found to be dependent on the initial starting condition (i.e., outward or inward).

4. Symmetry-breaking behaviors at large gap ratios

In region V of the phase diagram (which lies above the neutral curve with a high gap ratio and an intermediate Reynolds number), a symmetric wake pattern, with two vortex streets keeping a sufficiently large distance from each other, is eventually developed. More interestingly, this ultimate state can be reached by two different paths, depending on the initial condition specified. For the initial condition with inward starting, the evolution of wake structure is shown in Fig. 8. It is

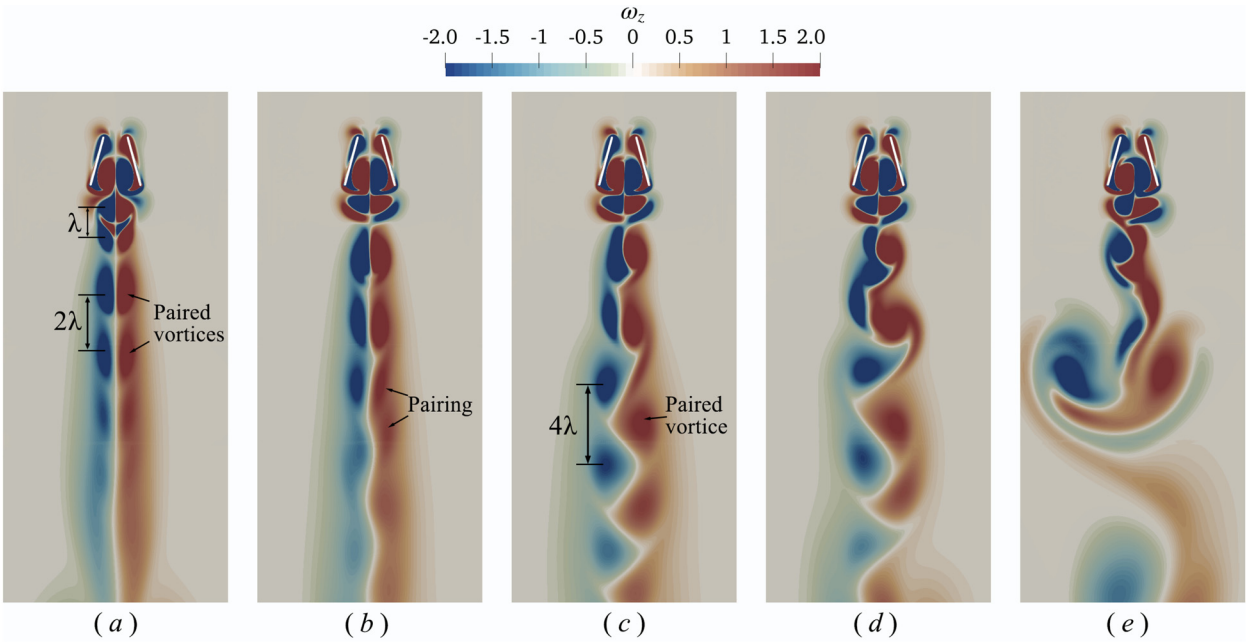

FIG. 6. Vorticity fields at various time instants in the wake evolution of ($g = 0.6$, $Re = 200$) (a case located in region III of Fig. 3): (a) $t = 30T$; (b) $t = 50T$; (c) $t = 80T$; (d) $t = 115T$; and (e) $t = 250T$. 2λ and 4λ denote the wavelengths of the vortex street after undergoing the first and second vortex-pairing processes, respectively.

seen that a temporally symmetric wake pattern featured by two close-set vortex streets is established after the transient phase [see Fig. 8(a)]. Symmetry breaking is then triggered and an incipient secondary vortex street is formed [see Figs. 8(b) and 8(c)]. Unlike the symmetry-breaking behaviors of the cases in region II, here the secondary vortex street dissipates very rapidly and wake symmetry is eventually recovered after long-term evolution [see Fig. 8(d)]. For the initial condition of outward starting, the symmetric wake pattern with two separating vortex streets is established more easily, without undergoing the symmetry-breaking and symmetry-recovering processes (see Fig. 9).

In region VI of the phase diagram (with a high gap ratio and a high Reynolds number), an asymmetric wake with two swaying vortex streets is observed (see Fig. 10). This ultimate state can also be reached by two different paths, depending on the initial condition. For the initial condition of inward starting, the wake undergoes two symmetry-breaking processes. First, a temporally symmetric wake with two close-set vortex streets is developed after the transient phase [similar to the one shown in Fig. 8(a)]. Such wake is unstable and subsequently undergoes the symmetry-breaking and symmetry-recovering processes (similar to the situation we have in region V).

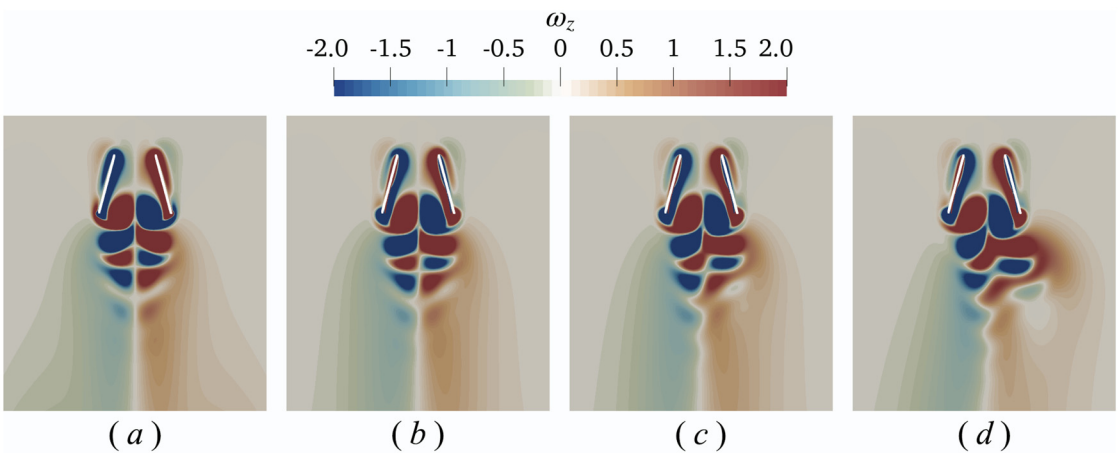

FIG. 7. Vorticity fields at various time instants in the wake evolution of ($g = 0.8$, $Re = 87.5$) (a case located in region IV of Fig. 3): (a) $t = 40T$; (b) $t = 70T$; (c) $t = 80T$; and (d) $t = 90T$.

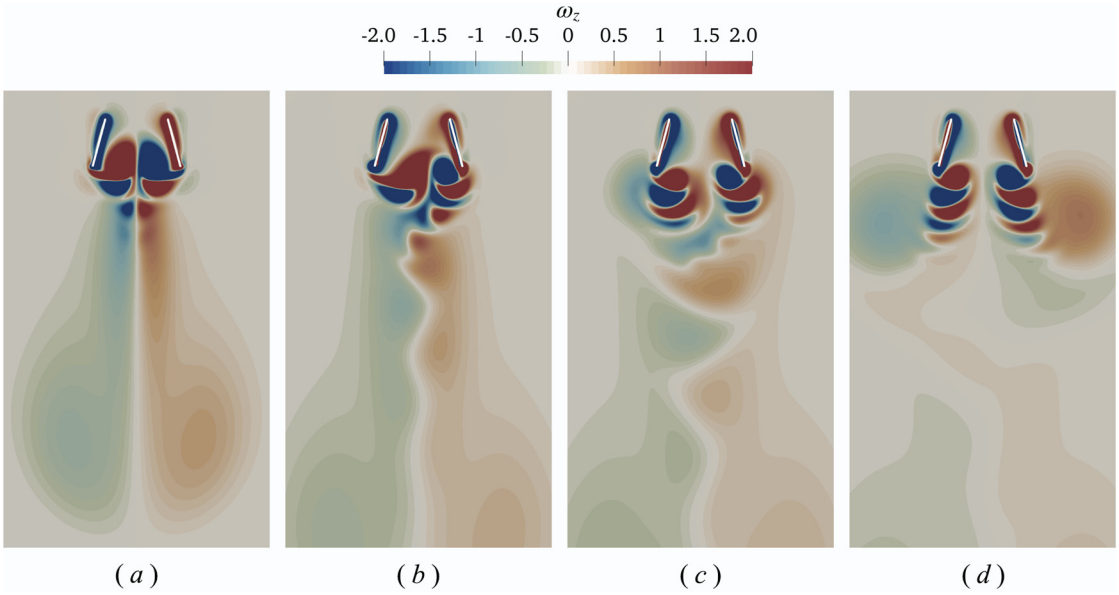

FIG. 8. Vorticity fields at various time instants in the wake evolution of ($g = 1.4$, $Re = 87.5$) (a case located in region V of Fig. 3): (a) $t = 40T$; (b) $t = 60T$; (c) $t = 70T$; and (d) $t = 90T$. The initial positions of the foils are at $\pm[\theta_0 + A_\theta]$ (inward starting).

Please note that the symmetry-breaking process observed here bears a resemblance to that observed in cases of region IV (rather than region V). In other words, the asymmetric wake pattern looks similar to that shown in Fig. 7(d). After the recovery of symmetry, a symmetric wake with two separating vortex streets is formed [similar to the ones shown in Figs. 8(d) and 9(d)]. However, unlike the situation we have in region V, such a wake is unstable, and symmetry breaking is triggered a second time. This eventually leads to the emergence of two separating vortex streets with in-phase swaying motion. For the initial condition of outward starting, a temporarily symmetric wake with two separating vortex streets is established soon after the transient phase. This is followed by the symmetry-breaking process which directly results in the emergence of two vortex streets with in-phase swaying motion. In other words, the symmetry-breaking and symmetry-recovering phases aforementioned are bypassed. The ultimate wake pattern observed here looks very similar to that reported in the studies on vortex shedding from two side-by-side circular cylinders.[4,5,65] The marked difference between these two scenarios is that the vortex streets are of thrust-producing (reversed Kármán) type here, whereas the vortex streets are of drag-producing (Kármán) type in those works.

B. Floquet stability analysis

In this section, the instability mechanisms of wake symmetry breaking are unveiled by performing Floquet analysis. To this end, some cases corresponding to the distinct symmetry-breaking behaviors depicted in Sec. V A are selected.

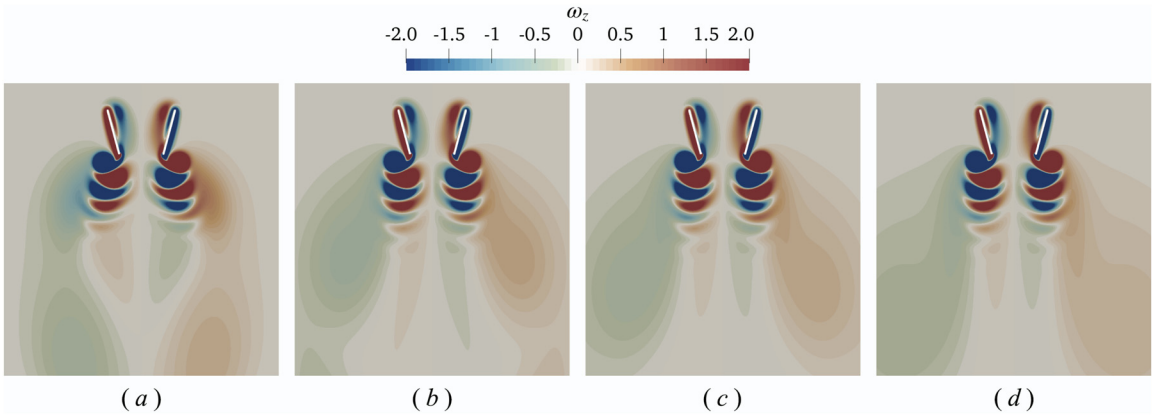

FIG. 9. Vorticity fields at various time instants in the wake evolution of ($g = 1.4$, $Re = 87.5$) (a case located in region V of Fig. 3): (a) $t = 40T$; (b) $t = 60T$; (c) $t = 70T$; and (d) $t = 90T$. The initial positions of the foils are at $\pm[\theta_0 - A_\theta]$ (outward starting).

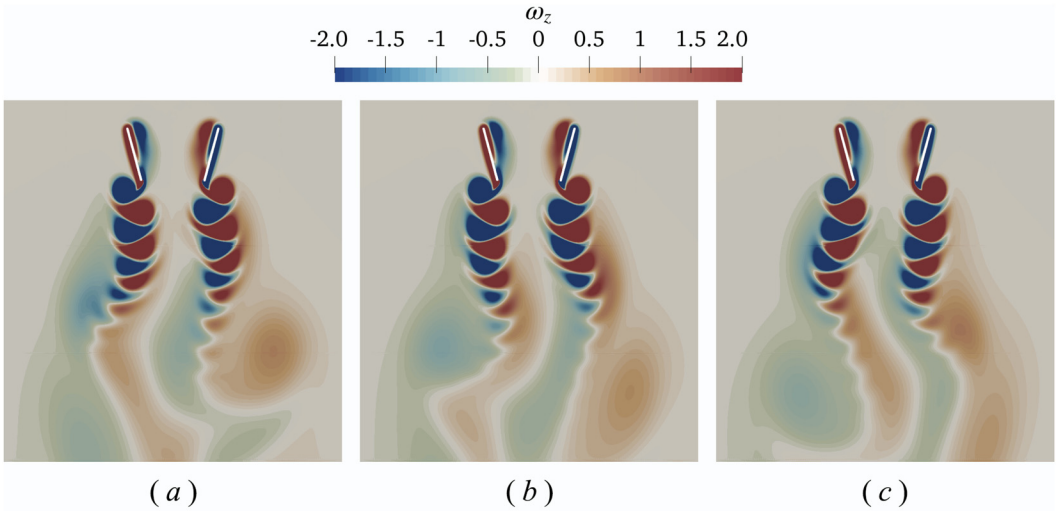

FIG. 10. Vorticity fields at various time instants in the wake evolution of ($g = 1.6$, $Re = 140$) (a case located in region VI of Fig. 3): (a) $t = 260T$; (b) $t = 265T$; and (c) $t = 270T$.

1. Region II

For the case of ($g = 0.6$, $Re = 150$) (which is located in region II), a complex-conjugate pair of Floquet multipliers crossing the unit circle, i.e., $\mu = 0.609 \pm 0.902i$, is obtained. This indicates that the symmetry-breaking instability associated with the wake is of quasiperiodic (QP) type.[12,13]

The base flow, real, and imaginary parts of the leading Floquet eigenfunction, base flow plus perturbation, and DNS at one specific phase point are illustrated in Fig. 11. Here, the flow fields are visualized by using *vorticity* contours. The vorticity contours shown in Fig. 11(a) indicate that the base flow possesses the symmetric property depicted in (2). As that shown in Figs. 11(b) and 11(c), the eigenfunction possesses the anti-symmetric property depicted in (3). Thus, the combination of eigenfunction with base flow produces an asymmetric flow field. In other words, the perturbation of leading Floquet eigenfunction breaks the reflection symmetry of the flow field if initiated with the base flow. In order to better explain the connection between the eigenfunction and the DNS result, the combination of base flow with real part of the leading Floquet eigenfunction is shown in Fig. 11(d). The flow field from DNS at an early stage of symmetry breaking is also provided in Fig. 11(e) for comparison. Here, "early stage of symmetry breaking" can be precisely defined by delineating between distinct phases of wake evolution (see Sec. V C). Since the magnitudes of eigenfunctions are smaller than those of the base flows by one or two orders for all cases considered here, they are multiplied by a factor with the magnitude ranging from 20 to 60, before combining with the base flow. This multiplying factor is first estimated as an exponential function of time by using the Floquet multiplier. A small adjustment to it is then made for achieving a better match between the superimposed solutions and DNS results. By comparing Fig. 11(d) with Fig. 11(e), it is seen that the symmetry-breaking behavior obtained in DNS can be successfully predicted by using linear stability analysis.

From the eigenfunction vorticity fields shown in Figs. 11(b) and 11(c), a large-scale flow structure with alternately positive and negative vorticities is clearly visible in the far wake. The presence of such flow structure is linked with the formation of secondary vortex street in DNS. The wavelength of this flow structure is much larger than those of the primary vortex street. This implies that the frequency of the secondary vortex street is much lower than that of the primary one.

Here, we also compare the secondary frequency predicted by the linear stability analysis with that from the DNS result. The period of this secondary vortex street T_s can be estimated from the argument of complex Floquet multiplier (θ),[13] namely, $T_s = 2\pi T/\theta \approx 6.45T$. Thus, the secondary frequency is approximately $0.155f$. From the power spectral density (PSD) plot for the horizontal force coefficient obtained in DNS, a secondary frequency of $0.143f$ can be identified [see Fig. 12(b)]. This value is reasonably close to that predicted by the linear stability analysis. From the PSD plot for the horizontal force coefficient, a "frequency splitting" phenomenon is also observed. To be more specific, two frequencies which are very close to the primary frequency f are identified. Furthermore, the frequency splitting phenomenon is also observed in the higher-order harmonics of the primary frequency. In the study of wake produced by an oscillating cylinder, it was suggested that the emergence of a secondary frequency in the symmetry-breaking process was the consequence of "beating" between the two close-set frequencies around the primary one.[14]

2. Region III

For the case of ($g = 0.6$, $Re = 200$), which is located in region III, a base flow with vortex pairing (i.e., with a period of $2T$) is naturally obtained by imposing the symmetric boundary condition. An unpaired base flow (with a period of T) can also be obtained if a time-delay term for suppressing vortex pairing is added to the governing equation.[64] It is reasonable to conjecture that the unpaired base flow is unstable and susceptible to the period-doubling instability. Since such

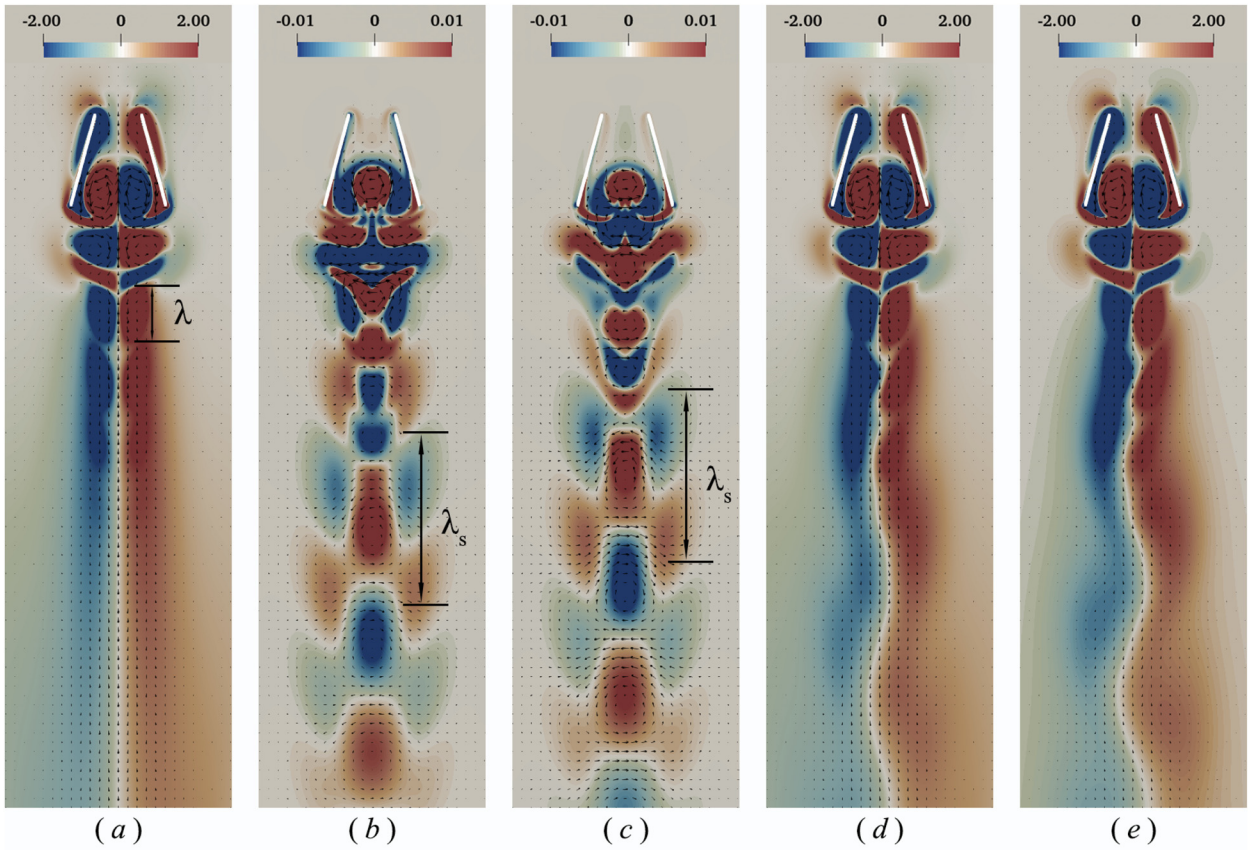

FIG. 11. Vorticity contours and velocity vectors obtained in linear stability analysis and nonlinear simulation (DNS) for the case of ($g = 0.6$, $Re = 150$): (a) Basic flow; (b) and (c) real and imaginary parts of the leading Floquet eigenfunction; (d) basic flow plus perturbation; and (e) DNS result ($t = 70T$). In (d), the perturbation is multiplied by a factor of 60 before combining with the base flow. All pictures are plotted at the same phase point.

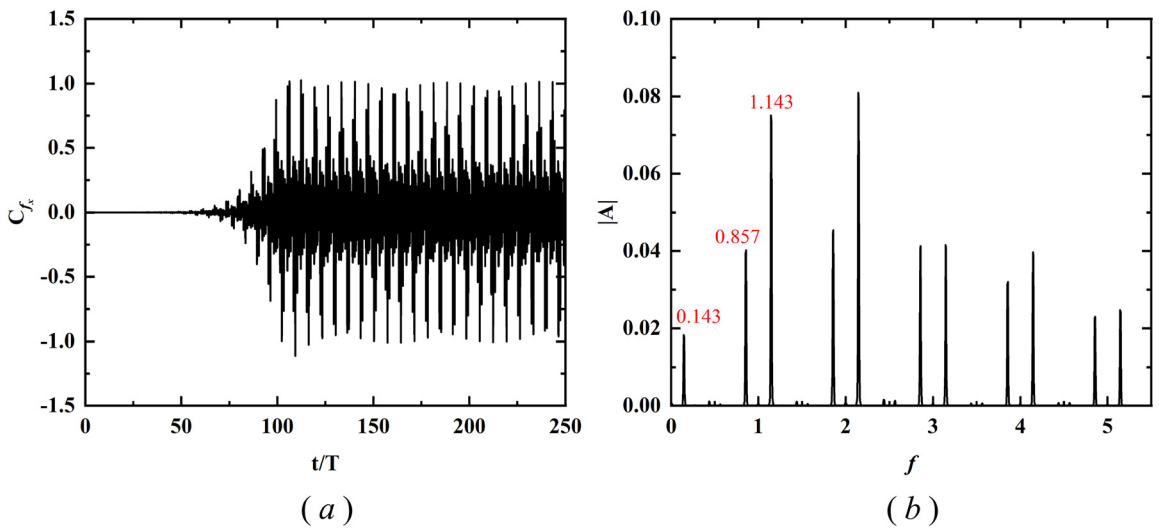

FIG. 12. The time history of horizontal force coefficient (a) and its power spectral densities (PSD) (b) for the case of ($g = 0.6$, $Re = 150$). The PSD in (b) is obtained by performing FFT on the time series of (a) over the interval [$150T$, $250T$].

period-doubling instability is irrelevant to the symmetry-breaking/symmetry-preserving behaviors of the wake, linear stability analysis on such base flow is beyond the scope of the present study.

Floquet stability analysis indicates that the paired base flow (with a period of $2T$) is also unstable. A real Floquet multiplier crossing the unit circle on the negative x axis, i.e., $\mu = -1.336$, is obtained. This indicates that symmetry breaking in the wake is induced by another period-doubling instability. From the eigenfunction vorticity field shown in Fig. 13(b), it is observed that the large-scale flow structure in the far wake possesses a wavelength which is (approximately) twice of the vortex streets in the (paired) base flow. From Figs. 13(c) and 13(d), it is seen that linear stability analysis can be used to reproduce the symmetry-breaking behavior obtained in DNS. The time history of horizontal force coefficient and its power spectral density (PSD) are shown in Fig. 14. From the PSD plot, a frequency which is one-quarter of the primary frequency can be identified. This further suggests that the symmetry-breaking phenomenon and the period-doubling instability are closely related to each other.

3. Region IV

For the case of ($g = 0.8$, $Re = 87.5$) (which is located in region IV), a real Floquet multiplier crossing the unit circle, i.e., $\mu = 1.1583$, is obtained. This indicates that the symmetry-breaking instability associated with the wake is of synchronous (S) type.[12,13] The base flow, leading Floquet eigenfunction, base flow plus perturbation, and DNS result at one specific phase point are illustrated in Fig. 15. Similar to the previous cases, the eigenfunction possesses the anti-symmetric property and the perturbation of leading Floquet mode breaks the symmetry of the flow field if initiated with the base flow. The symmetry-breaking behavior predicted by the linear stability analysis is also inconsistency/consistent with the DNS result [as shown in Figs. 15(c) and 15(d)]. Unlike the previous cases, flow structure with alternately positive and negative signs does not show up in the eigenfunction vorticity field. It implies that no second frequency emerges during the growth of wake asymmetry. This is further supported by the time history of horizontal force coefficient and its power spectral density (PSD) (as shown in Fig. 16). Only the

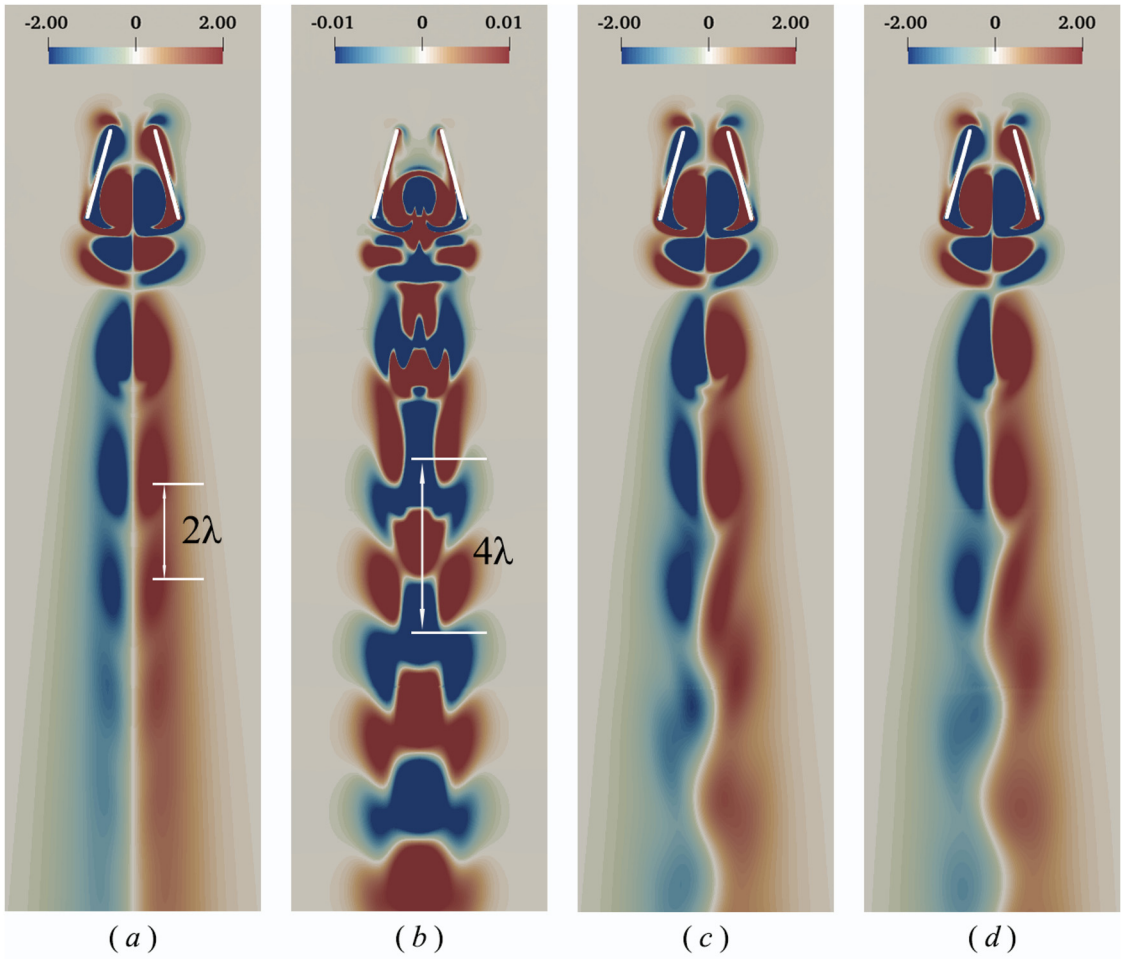

FIG. 13. Vorticity contours obtained in linear stability analysis and nonlinear simulation (DNS) for the case of ($g = 0.6$, $Re = 200$): (a) Basic flow; (b) (real) leading Floquet eigenfunction; (c) basic flow plus perturbation; and (d) DNS result ($t = 52T$). In (c), the perturbation is multiplied by a factor of 20 before combining with the base flow. All pictures are plotted at the same phase point.

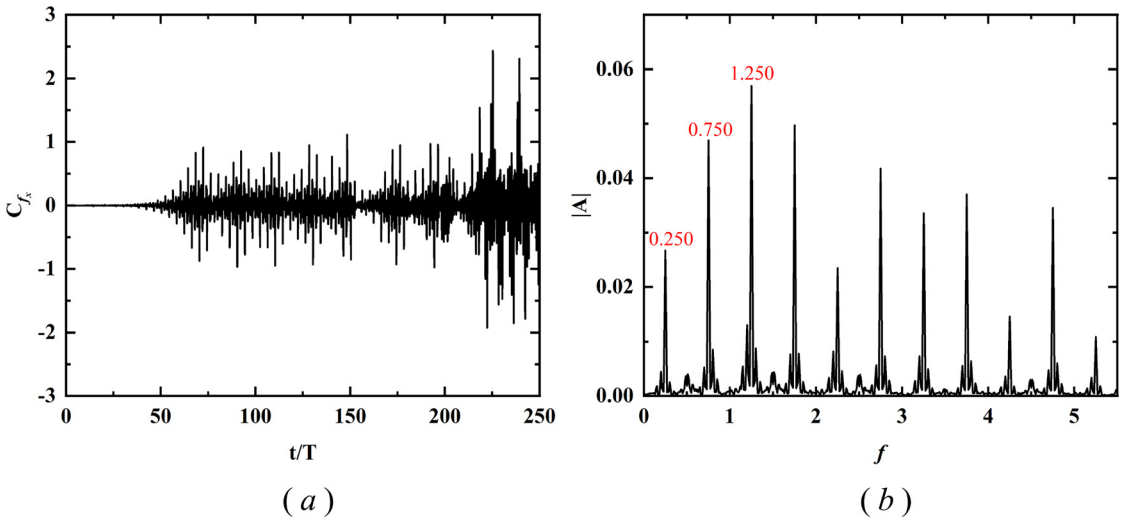

FIG. 14. The time history of horizontal force coefficient (a) and its power spectral densities (PSD) (b) for the case of $(g = 0.6,\ Re = 200)$. The PSD in (b) is obtained by performing FFT on the time series of (a) over the interval $[50T,\ 150T]$.

primary (flapping) frequency and its high-order harmonics can be identified in the PSD plot.

4. Region V

For the case of $(g = 1.4,\ Re = 87.5)$ (which is located in region V), two base flow solutions are obtained (see Fig. 17). The base flow solution with two close-set vortex streets is termed the "compact" type [Fig. 17(a)], while the solution in which two vortex streets keep a sufficiently large distance from each other is termed the "incompact" type [Fig. 17(b)]. The former one is obtained with the initial condition of inward starting, while the latter one is obtained with the initial condition of outward starting. (It is interesting to note that for the cases which lie below the neutral curve with a large gap ratio, only incompact base flows are obtained regardless of the initial condition. The results of Floquet stability analysis indicate that such base flows are always stable.)

The incompact base flow for case $(g = 1.4,\ Re = 87.5)$ is stable. The compact base flow is unstable, and a complex-conjugate pair of Floquet multipliers crossing the unit circle, i.e., $\mu = 0.6299 \pm 1.0863$ i, is obtained. The base flow, real and imaginary parts of the leading Floquet eigenfunction, base flow plus perturbation and DNS result at one specific phase point are illustrated in Fig. 18. The eigenfunction vorticity field shares some similarities with that of case $(g = 0.6,\ Re = 150)$. A large-scale flow structure with alternatively positive and negative vorticities is also visible in the far wake. This flow structure possesses a much larger wavelength than that of the near-wake flow structure. Despite the similarities, notable differences in the eigenfunction vorticity fields of the two cases are also observed. In this case, the magnitude of eigenfunction vorticity in the far wake is much smaller and the vorticity field decays much faster in distance from the trailing ends.

The secondary period T_s can be estimated by the argument of the complex Floquet multiplier (θ) as: $T_s = 2\pi T/\theta \approx 6.01T$. Thus, the secondary frequency is approximately $0.166f$, which is much lower than the primary (driving) frequency. Here, we also compare this predicted frequency from the linear stability analysis with that from the DNS result. The time history of horizontal force coefficient and its power spectral density (PSD) are shown in Fig. 19. The secondary frequency identified from the PSD plot is $0.160f$, which matches well with that obtained by the linear stability analysis. From the PSD plot, the frequency splitting phenomenon [similar to that observed in case $(g,\ Re) = (0.6, 150)$] is also observed.

It should be reminded that some special attention needs to be paid to cases in region V, where two base flow solutions with different stability properties exist. Contrasting symmetry-breaking/preserving behaviors are observed if the flow fields in DNS are initialized with base flows of different type.

5. Region VI

For the case of $(g = 1.6,\ Re = 140)$ (which is located in region VI), two base flow solutions (i.e., compact and incompact types) are obtained, as similar to the situation we have in region V. The compact base flow can be obtained by using the initial condition of inward starting. To obtain the incompact base flow, it is necessary to begin with a case with a lower Reynolds number (e.g., a case which is located in region V) and the initial condition of outward starting. The Reynolds number is then gradually increased until the targeted one is reached.

The results of Floquet stability analysis indicate that in this case both types of base flow are unstable. For the compact base flow, a real Floquet multiplier crossing the unit circle, $\mu = 1.7602$, is obtained. The Floquet eigenfunction looks very similar to that of case $(g = 0.8,\ Re = 87.5)$ (see Fig. 15). For the incompact base flow, a complex-conjugate pair of Floquet multipliers crossing the unit circle, $\mu = 0.9514 \pm 0.3907$ i, is obtained. The secondary frequency is approximately $0.062f$. The base flow, real and imaginary parts of the Floquet eigenfunction, base flow plus perturbation and DNS flow field at one specific phase point, are shown in Fig. 20. Similar to that obtained with the compact base flow, anti-symmetric property of the eigenfunction accounts for the occurrence of wake symmetry breaking.

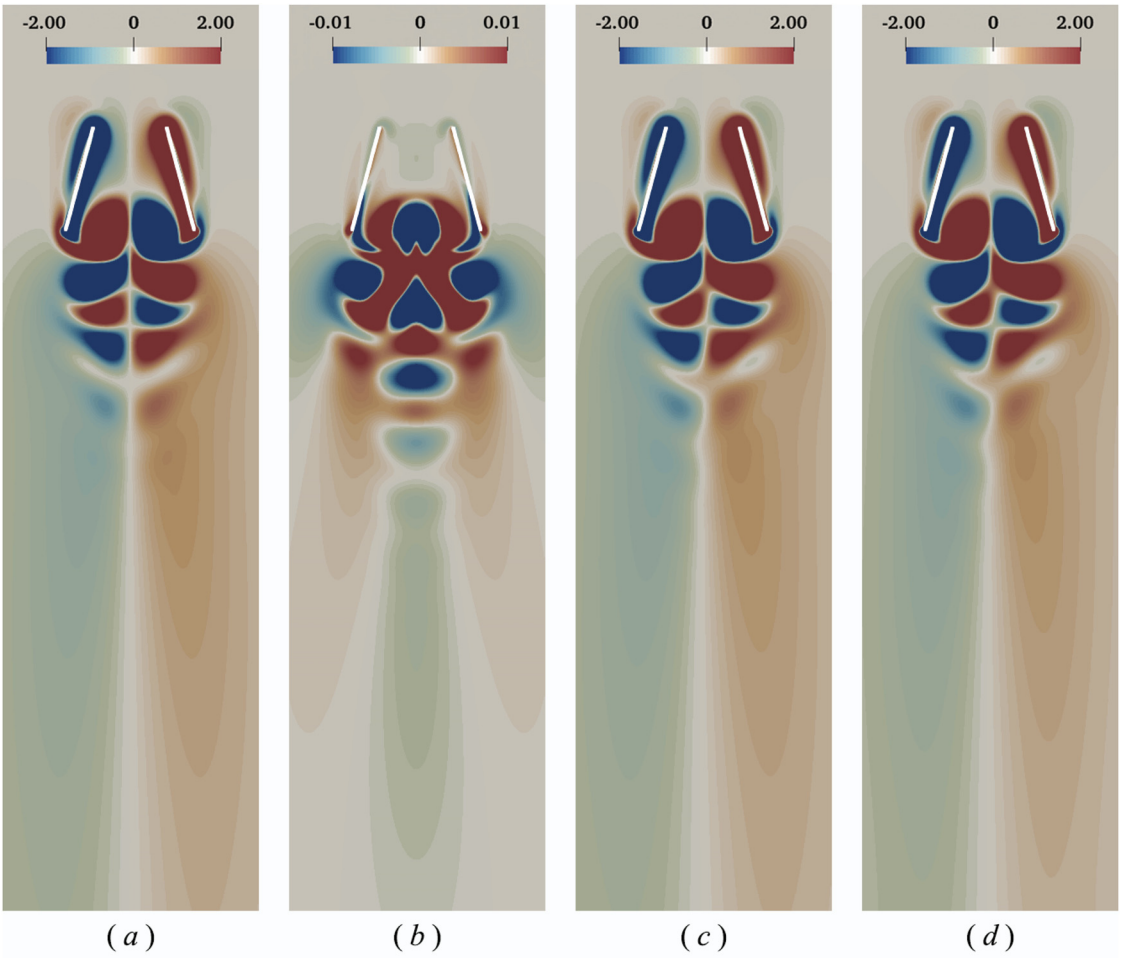

FIG. 15. Vorticity contours obtained in linear stability analysis and nonlinear simulation (DNS) for the case of ($g = 0.8$, $Re = 87.5$): (a) Basic flow; (b) (real) leading Floquet eigenfunction; (c) basic flow plus perturbation; and (d) DNS result ($t = 75T$). In (c), the perturbation is multiplied by a factor of -25 before combining with the base flow. All pictures are plotted at the same phase point.

However, the distribution of eigenfunction vorticity differ significantly from the one obtained with the compact base flow. Here, a three-column (instead of one-column) flow structure with alternatively positive and negative vorticities is observed in the far wake. As shown in Figs. 20(d) and 20(e), base flow plus perturbation is inconsistency/consistent with the DNS result, where two separating vortex streets in swaying motion are formed. From the power spectral density (PSD) plot for the horizontal force coefficient, a secondary frequency of $0.067f$ can be identified [see Fig. 21(b)]. This result matches well with that obtained by the linear stability analysis. From the PSD plot, the frequency splitting phenomena near the primary (driving) frequency and its higher-order harmonics are also observed.

6. Bifurcation types

Based on the Floquet multipliers obtained in cases slightly above the neutral curve, this curve can be divided into three segments (see Fig. 3). For segments A–B and C–D, a pair of complex-conjugate Floquet multipliers is obtained. This indicates the occurrence of Neimark–Sacker bifurcation when crossing the neutral curve. In segment B–C, a real Floquet multiplier is obtained. This indicates the occurrence of saddle-node bifurcation when crossing the neutral curve. The two intersection points between different segments are ($g = 0.694$, $Re = 120.31$) and ($g = 1.125$, $Re = 86.72$), respectively. A vertical line which connects two horizontally oriented segments is observed at $g = 0.7$. The shape of this neutral curve shares some similarities with that of the neutral curve obtained in the study on two parallel Kármán wakes behind two side-by-side cylinders.[4] In both scenarios, the neutral curve is composed of several segments, and cusps are formed at the intersections between segment pairs.

The neutral curve determined by using linear stability analysis is generally in accordance with that predicted by using DNS. For cases located in different unstable regions and far from the neutral curve, distinct symmetry-breaking behaviors observed in DNS can also be rationalized using linear stability analysis. It is worthwhile to note that the partitioning of parameter space into regions is solely based on

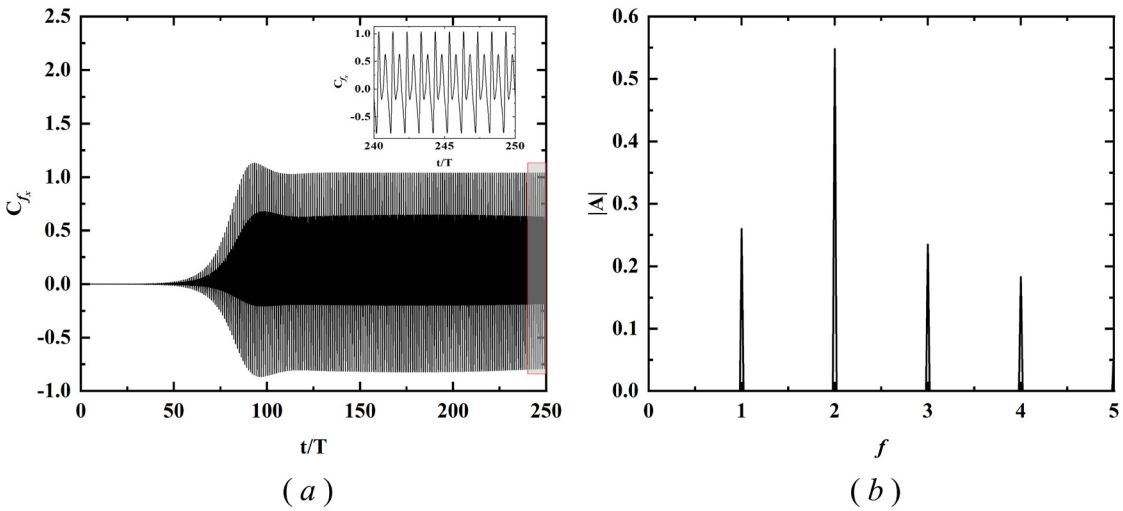

FIG. 16. The time history of horizontal force coefficient (a) and its power spectral densities (PSD) (b) for the case of $(g = 0.8,\ Re = 87.5)$. The PSD in (b) is obtained by performing FFT on the time series of (a) over the interval $[125T,\ 250T]$.

distinct behaviors observed in the time course of wake evolution. Such partitioning cannot be used to categorize the bifurcation types in the unstable regions. For identifying and tracing bifurcations in the entire parametric space of (g, Re), a careful codimension-two bifurcation analysis needs to be performed.[4] No such attempt is made in the present study.

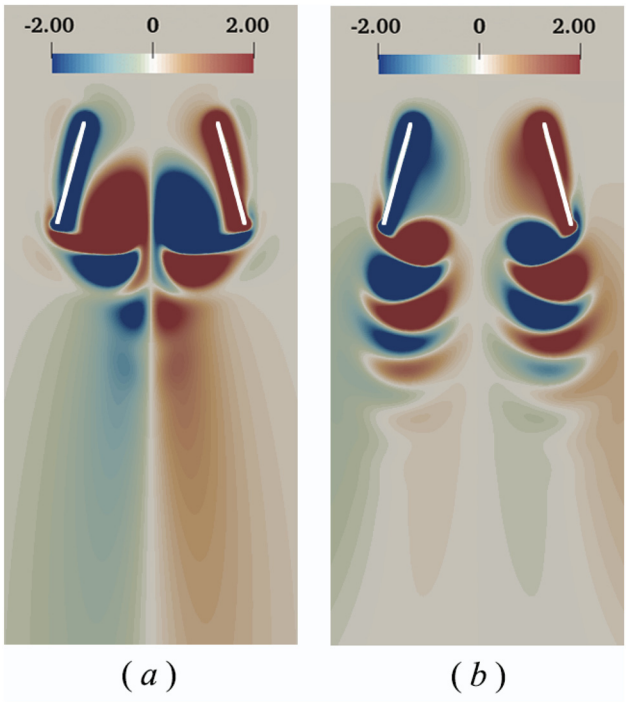

FIG. 17. Vorticity contours of basic flows for the case of $(g = 1.4,\ Re = 87.5)$ obtained with inward starting (a) and outward starting (b).

C. Dynamic mode decomposition

In Sec. V B, Floquet stability analysis is used to unveil the physical mechanisms of wake symmetry breaking observed in some selected cases. In this section, DMD is applied to these cases for providing more insight into this phenomenon.

The DMD analysis performed on the data of $(g = 0.6,\ Re = 150)$ (region II) and $(g = 0.8,\ Re = 87.5)$ (region IV) is detailed first. Data selection is done by following the approach proposed in some Refs. 53 and 66. We first delineate between distinct phases of wake evolution by examining the time history of the magnitude of lateral-force coefficient (see Fig. 22). A linear transient phase with exponential growth of $|C_{fx}|$ and a nonlinear saturation phase can be identified. Only the time-resolved DNS data from the first phase is used to perform DMD analysis. This is because we are interested in the linear dynamics of the system immediately after the onset of instability. To be more specific, time intervals of $[40T,\ 60T]$ and $[40T,\ 70T]$ are used for the two cases, respectively. The sampling increment is set to $0.05T$. As a result, the total numbers of snapshots used in DMD analysis of the two cases are 400 and 600, respectively. It is found that the results of DMD analysis are barely affected if the numbers of snapshots are further increased.

Figure 23(a) shows the eigenvalues $\hat{\lambda}_j$ in complex plane for the case of $(g = 0.6,\ Re = 150)$. Here, only the eigenvalues of the modes whose amplitudes exceed 1% of the highest amplitude among all DMD modes are plotted. The energy spectrum of the DMD modes for this case is shown in Fig. 23(b).

Mode M_0 with $\hat{\lambda} = 0$ represents the time-invariant part of the system. Since the flow is generated by periodic motion and the free-stream velocity is zero, such mode is a spurious one due to numerical artifacts. An energetic M_0 mode identified here can be explained by the fact that periodicity condition is not strictly satisfied by the DMD data. This does happen if the time-resolved data are of multi-periodic nature and existing periods are not constant multiples of each other.

The frequencies of other neutrally stable modes (i.e., M_1, M_2, M_3, etc.) are the primary frequency f and its high-order harmonics. The

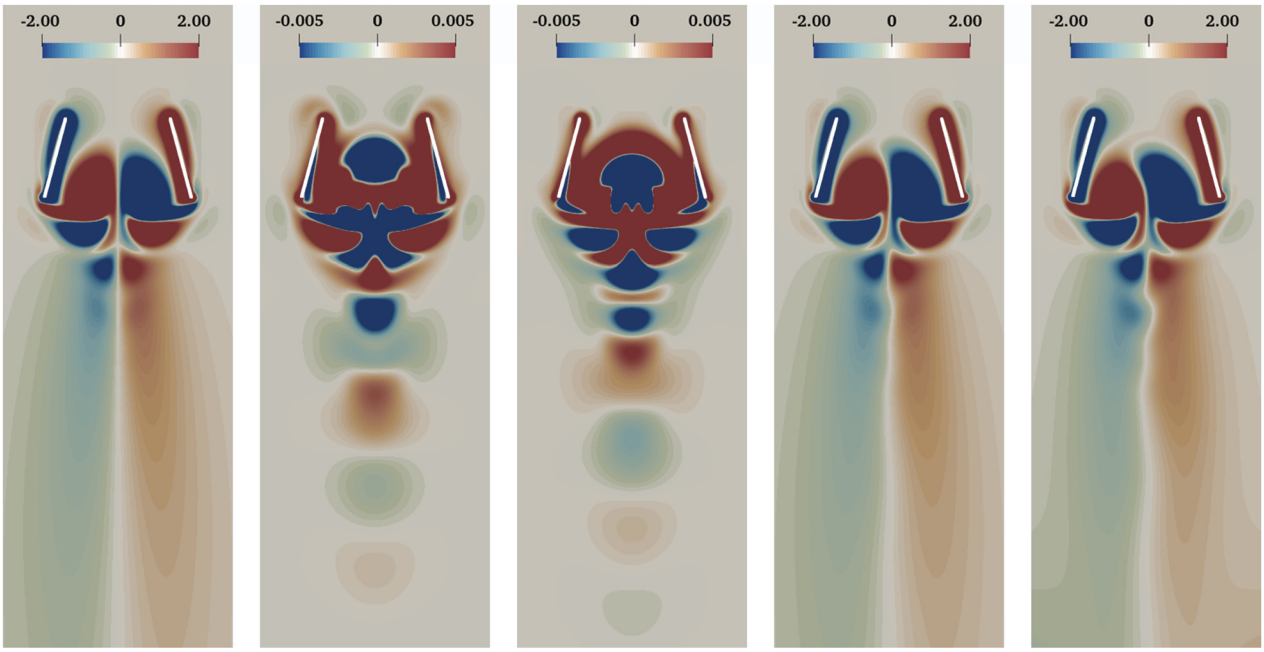

FIG. 18. Vorticity contours obtained in linear stability analysis and nonlinear simulation (DNS) for the case of ($g = 1.4$, $Re = 87.5$): (a) (Compact) Basic flow; (b) and (c) real and imaginary parts of the leading Floquet eigenfunction; (d) basic flow plus perturbation; and (e) DNS result ($t = 50T$). In (d), the perturbation is multiplied by a factor of 50 before combining with the base flow. All pictures are plotted at the same phase point.

flow fields of these modes possess the symmetric property depicted in (2). As one example, the flow field of the most energetic mode, M_1, is shown in Figs. 23(c) and 23(d). These neutrally stable modes can be regarded as the "symmetry-preserving" part of the system.

The unstable modes (i.e., M_1', M_2', M_3', etc.) are less energetic if compared with the neutrally stable ones. The frequencies of these modes are $f_s, f \pm f_s$, $2f \pm f_s$, etc., where f_s is a newly emerged frequency which is much lower than the primary one. In other words, the

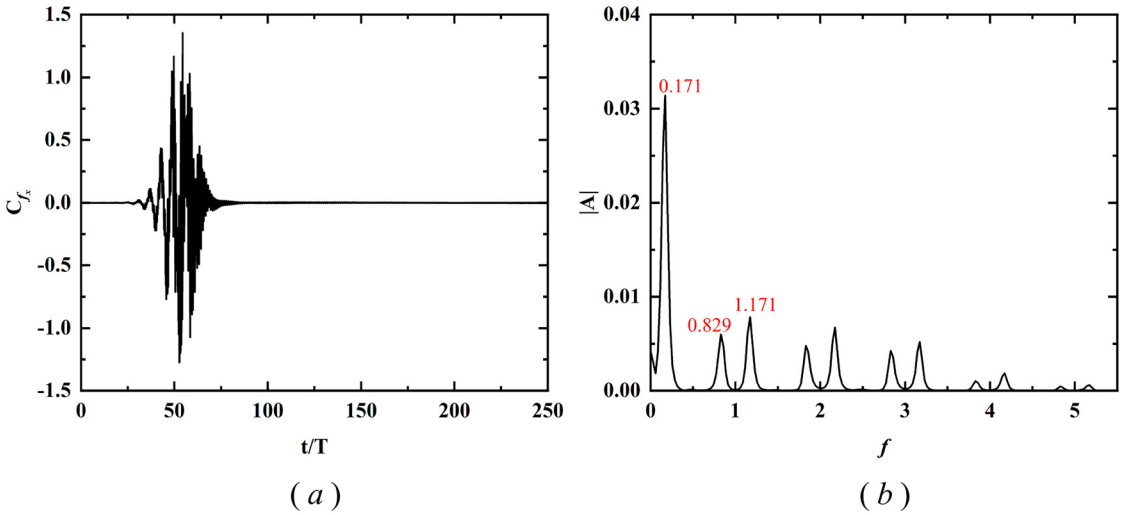

FIG. 19. The time history of horizontal force coefficient (a) and its power spectral densities (PSD) (b) for the case of ($g = 1.4$, $Re = 87.5$). The PSD in (b) is obtained by performing FFT on the time series of (a) over the interval [$20T$, $55T$].

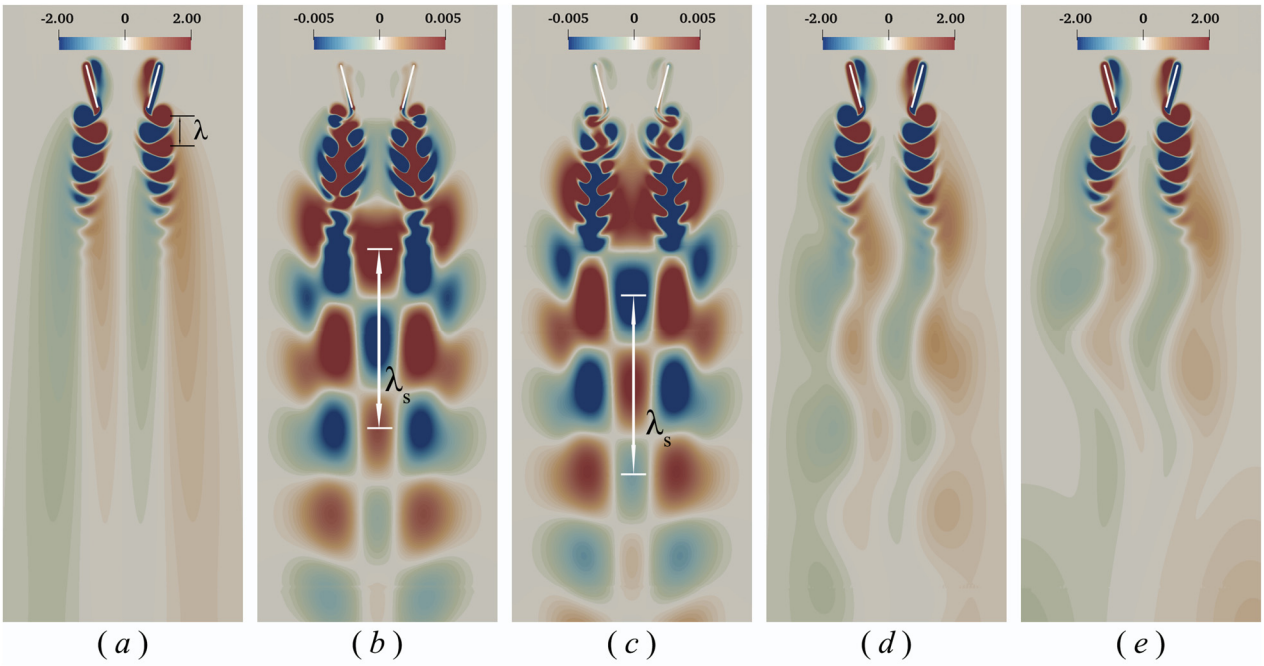

FIG. 20. Vorticity contours obtained in linear stability analysis and nonlinear simulation (DNS) for the case of ($g = 1.6$, $Re = 140$): (a) (Incompact) Basic flow; (b) and (c) real and imaginary parts of the Floquet eigenfunction; (d) basic flow plus perturbation; and (e) DNS result($t = 160T$). In (d), the perturbation is multiplied by a factor of 50 before combining with the base flow. All pictures are for the same phase point.

phenomenon of frequency splitting is observed near the primary frequency and its high-order harmonics. For this case, the frequency f_s is found to be $0.158f$, which is close to that of the leading Floquet mode identified in Floquet analysis. A newly emerged frequency signifies the appearance of a secondary flow structure. The flow fields of these unstable modes possess the anti-symmetric property depicted in (3) [see Figs. 23(e) and 23(f) for the flow field of mode M_1']. Clearly, the existence of unstable anti-symmetric modes can account for the occurrence of wake symmetry breaking.

Figure 24(a) shows the eigenvalues $\hat{\lambda}_j$ on complex plane for the case of ($g = 0.8$, $Re = 87.5$). Again, only the eigenvalues of the modes whose amplitudes exceed 1% of the highest amplitude among all

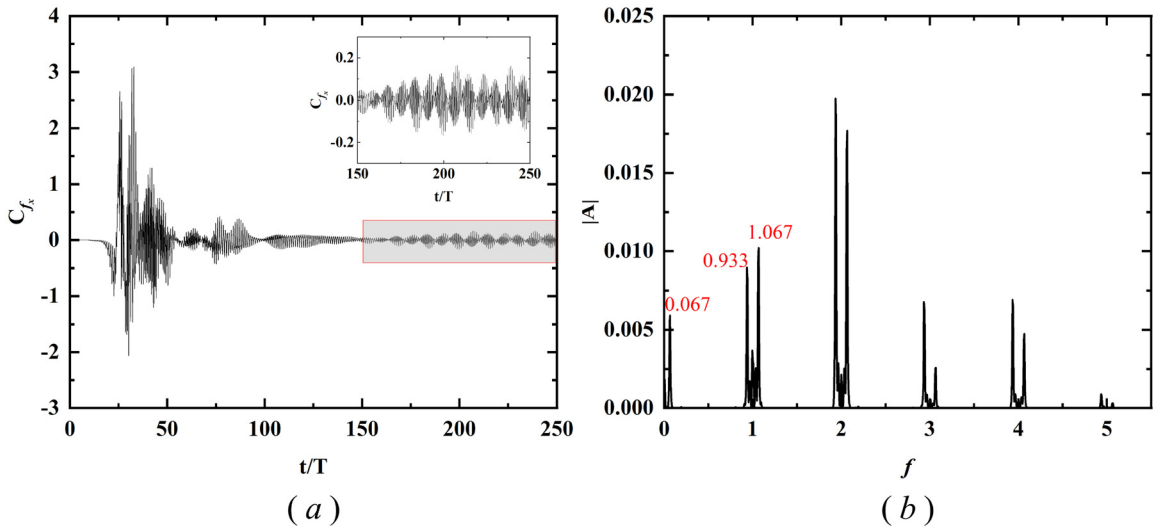

FIG. 21. The time history of horizontal force coefficient (a) and its power spectral densities (PSD) (b) for the case of ($g = 1.6$, $Re = 140$). The PSD in (b) is obtained by performing FFT on the time series of (a) over the interval [$150T$, $250T$].

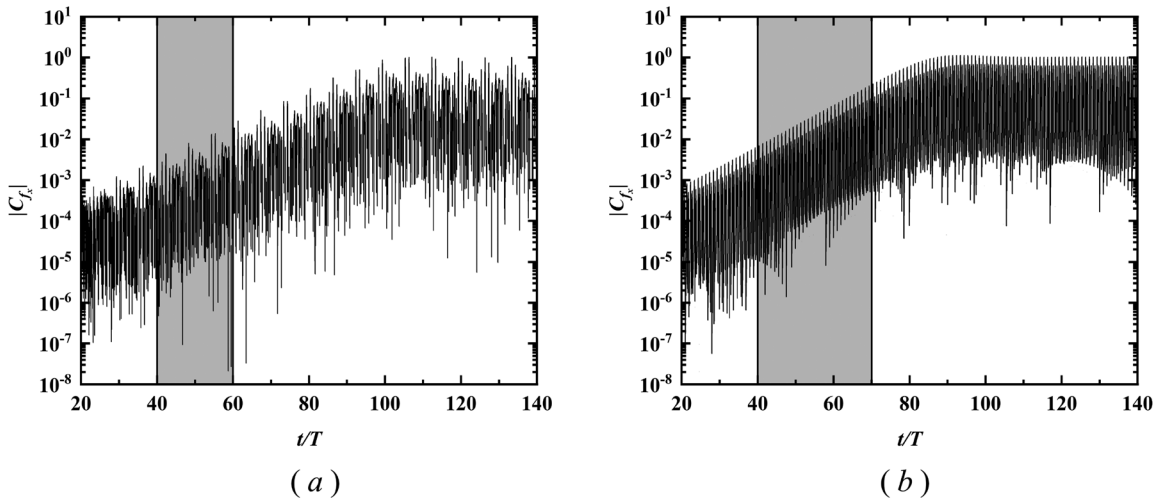

FIG. 22. The time histories of lateral-force coefficient magnitudes for (a) ($g = 0.6$, $Re = 150$) and (b) ($g = 0.8$, $Re = 87.5$). The time intervals used to select the data for DMD analysis are denoted by gray strips.

DMD modes are plotted. The energy spectrum of the DMD modes for this case is shown in Fig. 24(b).

The frequencies of neutrally stable modes (i.e., M_1, M_2, M_3, etc.) are also the primary frequency f and its high-order harmonics. Unlike the previous case, here the frequencies of unstable modes (i.e., M_1', M_2', M_3', etc.) are identical to those of the neutrally stable ones. Since no newly emerged frequency is introduced, the periodicity condition can be strictly satisfied by the DMD data. This explains why the energetic spurious mode with $\hat{\lambda} = 0$ is not observed. The flow fields of the neutrally stable and unstable modes possess the symmetric and anti-symmetric properties, respectively. To demonstrate this, the flow fields of mode M_1 and mode M_1' are shown in Figs. 24(c) and 24(d) and Figs. 24(e) and 24(f). The occurrence of wake symmetry breaking can also be explained by the existence of unstable anti-symmetric modes.

In addition to the two cases above, three cases from regions III, V, and VI (i.e., the cases discussed in Sec. V B) are also analyzed by using DMD. The aforementioned strategy is also adopted in preparing the data for DMD analysis. The findings from DMD analysis of these three cases are similar to those reported for the case of ($g = 0.6$, $Re = 150$) (region II). A newly emerged frequency which is much lower than the primary one is also identified. The frequencies are 0.248, 0.166, and 0.064, for the cases from regions III, V, and VI, respectively. These frequencies and those of the leading Floquet modes are sufficiently near to each other. The newly emerged frequencies signify the appearance of new flow structures such as paired vortices, secondary vortex street, or dual swaying vortex streets. The modes with newly emerged frequencies possess the anti-symmetric property and can account for the occurrence of wake symmetry breaking.

One interesting finding that is worthy of mentioning is provided here. For the case in region III, besides the unstable anti-symmetric mode with a newly emerged frequency which is approximately $0.25f$, another unstable *symmetric* mode with the frequency of $0.5f$ is also identified. The former one accounts for the wake symmetry breaking associated with period-doubling. The latter one accounts for the vortex-pairing process during which wake symmetry is still preserved. The unstable Floquet mode which possesses the symmetric property cannot be identified in Floquet analysis. This is because that the base flow used in Floquet analysis has already undergone the vortex-pairing process (see Sec. V B 2).

The consistency in the results of DMD and Floquet analyzes is unsurprising since both methods aim to approximate the linear dynamics of the system. One major difference between them lies in the reproduction of DNS results using mode superposition. DNS results can be reproduced accurately by a superposition of base flow and leading Floquet mode. However, tens of DMD modes are usually needed for reproducing the DNS results with an acceptable level of accuracy.

D. Influence of symmetry breaking on propulsive performance

The influence of wake symmetry breaking on propulsive performance is addressed in this section. It is evident that the lateral force which is produced as a result of symmetry breaking can pose some difficulties in maintaining straight-line swimming. However, how symmetry breaking affects the time-averaged thrust is still unclear. Here, we examine the time-averaged thrust coefficients as a function of gap ratio at three different Reynolds numbers (75, 100, 150), and the results are shown in Fig. 25.

From this figure, it is seen that at all three Reynolds numbers, due to the existence of ground effect the thrust coefficients are always larger than the asymptotic values at infinitely large gap ratio. (These asymptotic values are equivalent to the ones obtained in two isolated pitching foils.) Wake symmetry is preserved at all gap ratios at $Re = 75$. The thrust coefficient decreases monotonically with increasing gap ratio and gradually approaches the asymptotic value. This trend is in consistency with the that reported in some studies on a pair of side-by-side pitching foils and single pitching foil in ground effect.[30,41] At $Re = 100$, monotonicity of the function is not observed in the range of $0.7 \leq g \leq 1.2$, and the time-averaged thrust is somehow enhanced. Apart from this range, the thrust generation is still dominated by

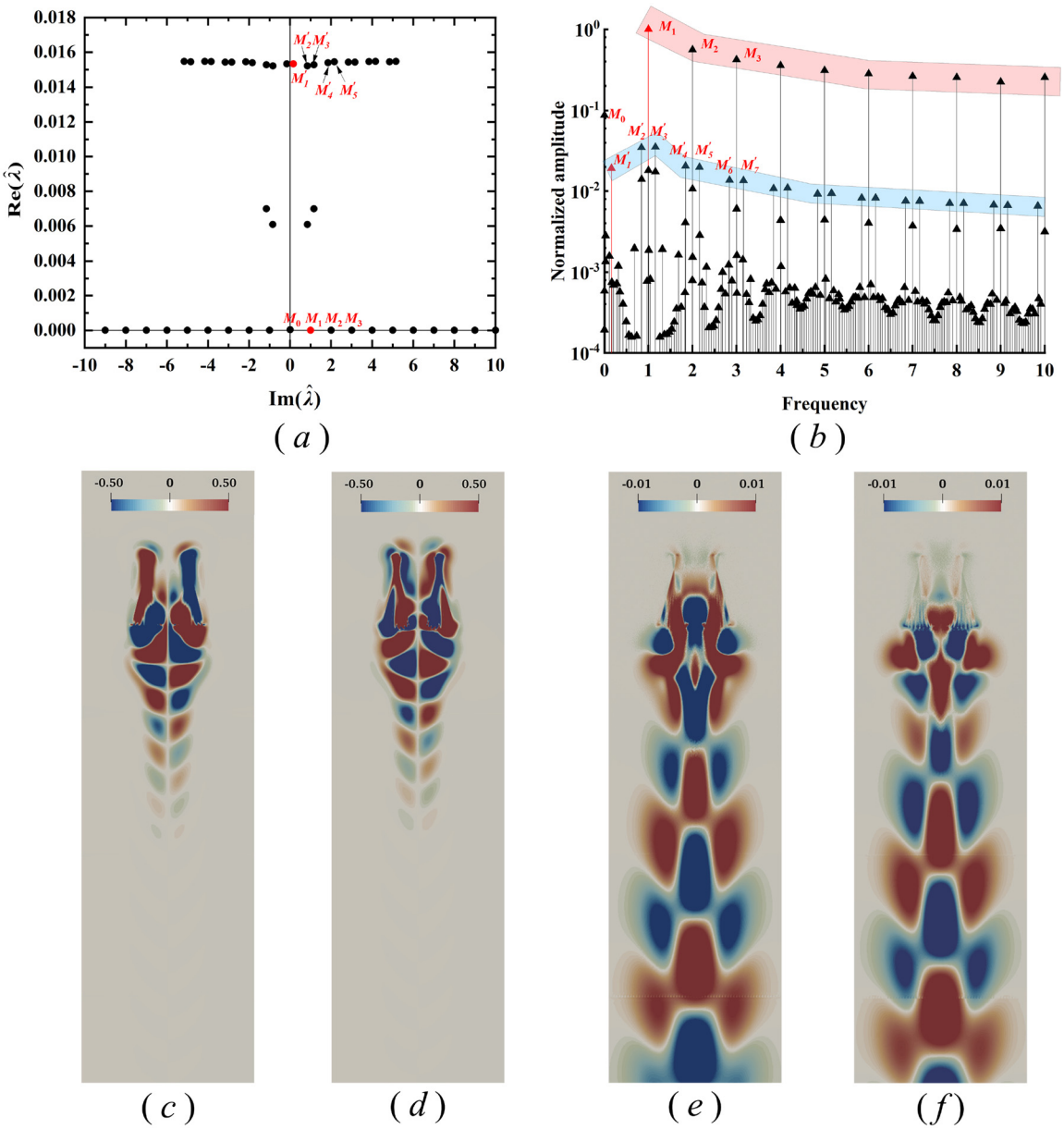

FIG. 23. The results of DMD analysis for the case of ($g = 0.6$, $Re = 150$): (a) Eigenvalues of DMD modes whose amplitudes exceed 1% of the highest amplitude among all modes; (b) energy spectrum of DMD modes; (c) vorticity contours of mode M_1 (real part); (d) vorticity contours of mode M_1 (imaginary part); (e) vorticity contours of mode M_1' (real part); and (f) vorticity contours of mode M_1' (imaginary part).

ground effect. For $Re = 150$, the trend of this function becomes more complex. Thrust enhancement is still observed in the range of $0.7 \leq g \leq 1.2$. At larger gap ratios, however, the thrust coefficient first increases with increasing gap ratio and then saturates.

To further elaborate how thrust generation is affected by the occurrence of symmetry breaking at Reynolds numbers 100 and 150, we compare the thrust coefficients obtained from DNS and from the base flow (see Fig. 26). The base flow can be regarded as a hypothetical solution if wake symmetry breaking has never been triggered. For cases in region V and region VI of Fig. 3, there exist two possible base flows (as shown in Fig. 17). Here, we use the incompact base flow to compute the thrust coefficient. The reason is that such type of base flow is more relevant to the ultimate state in DNS (see the wake evolution depicted in Secs. V B 4 and V B 5).

From Fig. 26, it is seen that in region IV the development of a deflected wake as a result of symmetry breaking can significantly enhance thrust generation. The maximal thrust increase can reach up to 30% and 35% for Re = 100 and Re = 150, respectively. Wake

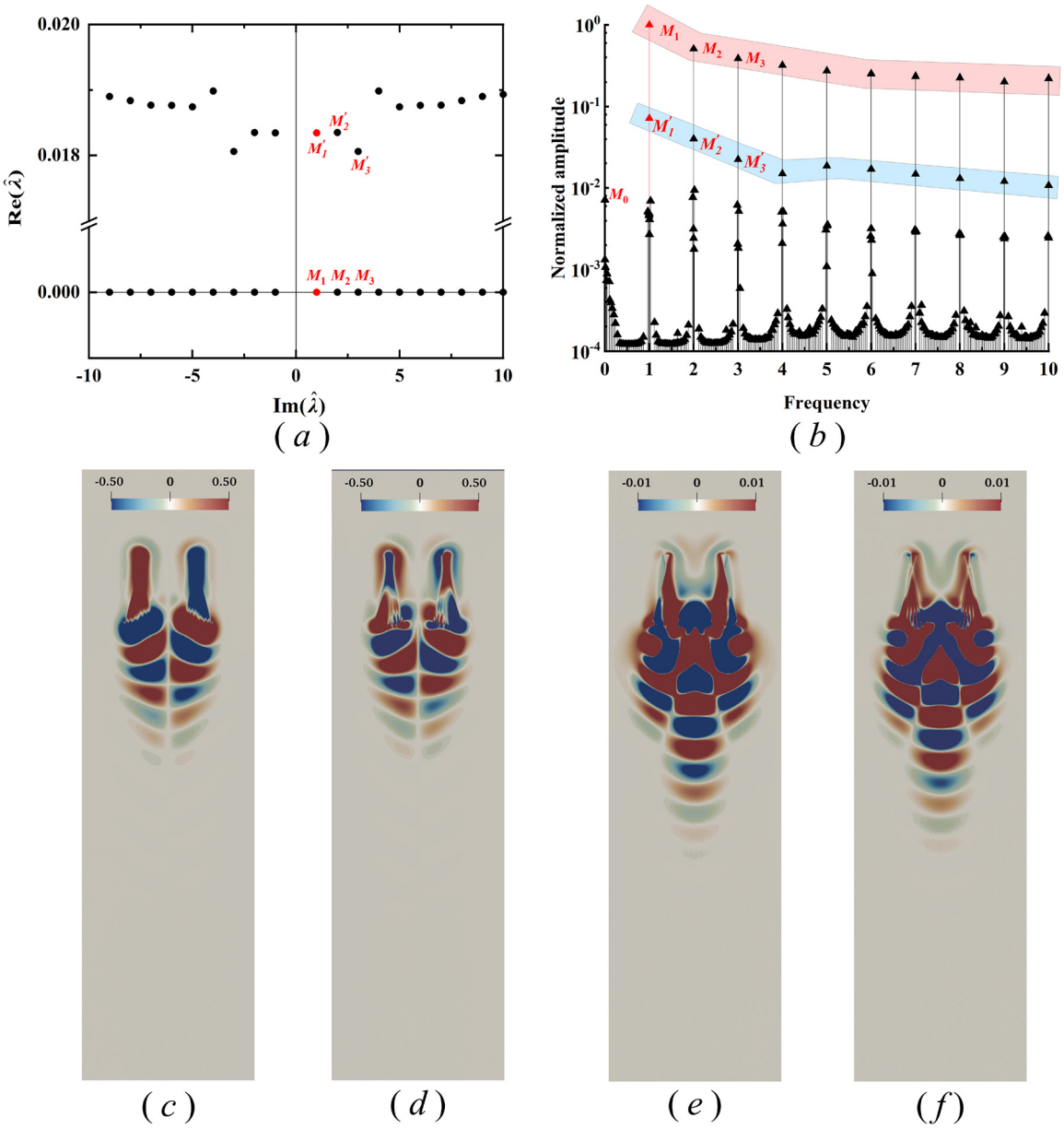

FIG. 24. The results of DMD analysis for the case of ($g = 0.8$, $Re = 87.5$): (a) Eigenvalues of DMD modes whose amplitudes exceed 1% of the highest amplitude among all modes; (b) energy spectrum of DMD modes; (c) vorticity contours of mode M_1 (real part); (d) vorticity contours of mode M_1 (imaginary part); (e) vorticity contours of mode M_1' (real part); and (f) vorticity contours of mode M_1' (imaginary part).

symmetry breaking of other types, such as that observed in region II (which is featured by a secondary vortex street), or in region VI (which is featured by two swaying vortex streets), has an insignificant effect on time-averaged force generation. The result of further investigation also indicates that symmetry breaking in region III (which is featured by vortex-pairing) hardly affects time-averaged thrust either. Such result is not shown here for brevity. From Fig. 26, we also notice that the thrust coefficients for the base flow sharply increase near the transition line between regions IV and V (or between regions IV and VI). This can be explained by the fact that the incompact base flow produces a higher thrust than the compact base flow.

Interestingly, the thrust enhancement due to wake symmetry breaking found here can be used to explain the phenomenon observed in a recent study on a self-propelled flyer in hovering flight.[37] In their work, the hovering state of the flyer was found to transit into a slowly rising state after wake symmetry breaking was triggered. The finding of the present study contrasts with that reported in a study on two side-by-side pitching foils subjected to a free-stream flow.[32] In their

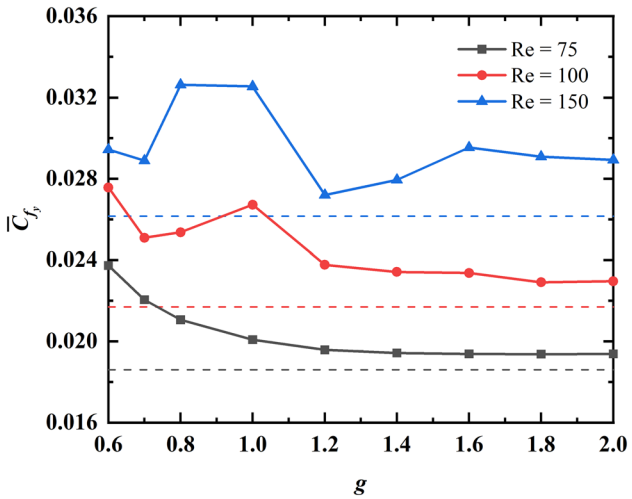

FIG. 25. Time-averaged thrust coefficients as a function of gap ratio for three different Reynolds numbers. The thrust coefficients are averaged over 250 flapping periods after the ultimate state in DNS is reached. The asymptotic thrust coefficients at infinitely large gap ratio are indicated by horizontal dashed lines.

work, it was found that wake symmetry breaking had almost no effect on time-averaged thrust. It seems that the influence of symmetry breaking on propulsive performance is strongly related to the magnitude of free-stream velocity. Further investigations are needed to clarify this issue.

VI. CONCLUSIONS

Numerical simulations are performed to examine the structures of the wakes generated by two anti-phase pitching foils at zero free-stream velocity, in a range of gap ratio $0.6 \leq g \leq 2.0$ and Reynolds number $70 \leq Re \leq 200$. The wake patterns are classified into six categories and described by six regions in the plane (g, Re). Wake symmetry is preserved in the region which lies below a neutral-stability curve. In the five regions above the neutral-stability curve, distinct symmetry-breaking behaviors are observed. At a small gap ratio and a moderate Reynolds number, the far wake is featured by the formation of a secondary reverse Kármán vortex street. If the Reynolds number increases further, the formation of secondary vortex street is accompanied by vortex-pairing and vortex-merging. At an intermediate gap ratio, vortex shedding is always synchronized with the flapping motion the wake is deflected toward one side. At a large gap ratio and a moderate Reynolds number, ultimately a symmetric wake with two separating vortex streets is obtained. At a large gap ratio and a high Reynolds number, an asymmetric wake consisting of two separating vortex streets with in-phase swaying motion is observed.

Floquet stability analysis is performed on some selected cases in the unstable regions. It has been revealed that the existence of unstable anti-symmetric Floquet modes leads to symmetry breaking in the wake. First, three cases located slight above the neutral-stability curve are analyzed. For the two cases with small and large gap ratios, the Floquet multipliers are complex-conjugate pairs crossing the unit circle. This suggests that the symmetry breaking is induced by a QP-type instability and a new frequency that differs from the primary one is introduced. For the case with intermediate gap ratios, a real Floquet multiplier crossing the unit circle on the positive x axis is obtained. This indicates that the symmetry breaking is induced by an S-type instability, and vortex shedding is always synchronized with the flapping motion. Second, two cases located far above the neutral-stability curve are also studied. For the case with a low gap ratio, a real Floquet multiplier which crosses the unit circle on the negative x axis is obtained. This indicates that the symmetry breaking is induced by a periodic-doubling instability. For the case with a high gap ratio, the Floquet multiplier is a complex-conjugate pair which crosses the unit circle and an ultralow secondary frequency is introduced in the symmetry-breaking process. In the leading eigenfunction vorticity field, a three-column flow structure with a very large wavelength is observed.

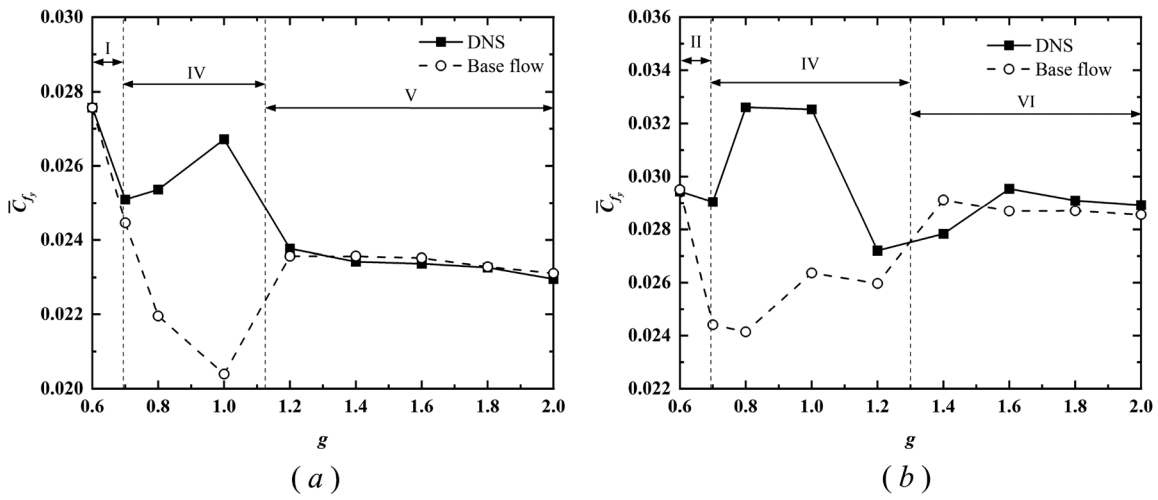

FIG. 26. Variation of time-averaged thrust coefficients with gap ratio: a comparison between thrust coefficients obtained from DNS and from the base flow: (a) $Re = 100$ and (b) $Re = 150$. The vertical dotted lines represent the borders between different sub-zones shown in Fig. 3.

DMD analysis is also performed on these selected cases for providing more insight into the symmetry-breaking phenomenon. The unstable DMD modes possess the anti-symmetric property and account for the occurrence of wake symmetry breaking. For the case in which symmetry breaking is induced by QP-type instability, one unstable DMD mode with a newly emerged frequency which is much lower than the primary one can be identified. This frequency and that of the leading Floquet mode are sufficiently near to each other. For the case in which symmetry breaking is induced by S-type instability, the frequencies of unstable DMD modes are the primary frequency and its high-order harmonics.

The influence of wake symmetry breaking on propulsive performance is then investigated. It is found that symmetry breaking induced by S-type instability, which is featured by a deflected wake, significantly enhances time-averaged thrust. Symmetry breaking induced by QP-type instability has an insignificant effect on time-averaged thrust.

By means of direct numerical simulation and modal analysis, the instability mechanisms for wake symmetry instability breaking in different regions of parameter space have been unveiled. In our future work, the influences of pivot-point position, flapping amplitude and equilibrium angle on the stability of the wakes will be explored. In additional, results from existing studies indicated that a free-stream flow can stabilize the wakes of dual-pitching-foil systems and make them less susceptible to symmetry-breaking instability. Thus, the instability mechanisms of the wakes at a nonzero free-stream velocity (i.e., a finite Strouhal number) also deserve further investigation. Another research avenue is sensitivity analysis of unstable modes and design of control strategies to suppress wake symmetry breaking.

ACKNOWLEDGMENTS

This research was funded by the National Science Foundation of China (NSFC), under the Grant Nos. 12172361, 11772338, 11372331, and 11988102 (Basic Science Center Program for Multiscale Problems in Nonlinear Mechanics). This research was also funded by the Chinese Academy of Sciences, under the Grant Nos. XDA22040203 and XDB22040104.

AUTHOR DECLARATIONS

Conflict of Interest

The authors have no conflicts to disclose.

Author Contributions

Zhiyu Zhang: Conceptualization (supporting); Data curation (lead); Formal analysis (equal); Investigation (equal); Methodology (equal); Software (lead); Validation (equal); Visualization (equal); Writing – original draft (equal); Writing – review & editing (supporting). **Xing Zhang:** Conceptualization (lead); Data curation (supporting); Formal analysis (equal); Funding acquisition (lead); Investigation (equal); Methodology (equal); Project administration (lead); Resources (lead); Supervision (lead); Writing – original draft (equal); Writing – review & editing (lead).

DATA AVAILABILITY

The data that support the findings of this study are available from the corresponding author upon reasonable request.

APPENDIX A: CODE VALIDATION TESTS

In order to validate the in-house flow solver and the linear stability code, we consider the flow around a two-dimensional oscillating cylinder in an initially quiescent fluid. A cylinder with diameter D undergoes a vertical oscillation of $y(t^*) = A\sin(2\pi f t^*)$ in a viscous fluid of kinematic viscosity ν, where A is the amplitude of the oscillation, t^* is the time, and f is the frequency of the oscillation. Two dimensionless numbers are used to describe the system: KC number $KC = 2\pi A/D$ and Stokes number $\beta = D^2 f/\nu$. This case has been investigated in experiments and simulations.[8,11–13]

The simulation is performed by using a uniform Cartesian mesh with the grid width of $D/50$ and a computational domain with the size of $[30D \times 30D]$. The boundary between the regions of symmetric and asymmetric flows in the parametric space (β, KC) is determined by direct numerical simulation and the result is shown in Fig. 27. From this figure, the boundary obtained by using the present flow solver agrees well with the experimental and numerical results from Refs. 8 and 11. Furthermore, two typical cases are chosen to validate the code for performing Floquet stability analysis. In Table I, the moduli of Floquet multipliers obtained by the present code are compared with the numerical result from Ref. 13. It is shown that the results are in good agreement with each other.

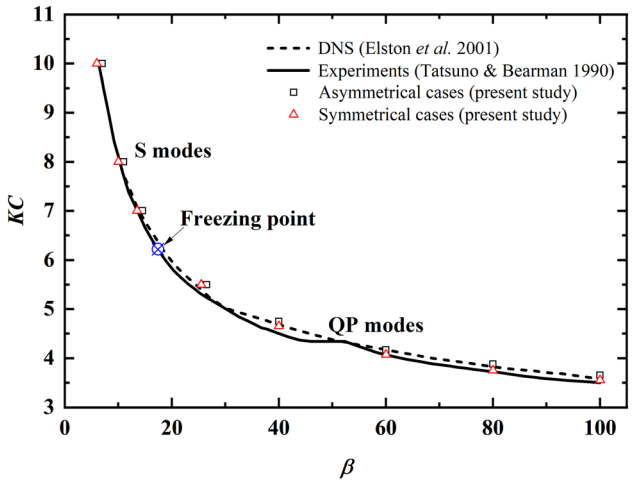

FIG. 27. Boundaries between the two-dimensional symmetrical flows and those with broken symmetry. Squares and triangles denote the asymmetrical cases and symmetrical cases obtained in the present study. The solid line and the dashed line denote the results of experiment[8] and simulation,[11] respectively. The "freezing point" is the dividing point of two different types of instability.[11]

TABLE I. Comparison of the moduli of Floquet multipliers computed using the present code with the reference solutions.

(KC, β)	Present	Reference value[13]	Relative error (%)
(40, 4.75)	1.1149	1.1064	0.77
(100, 3.65)	1.1700	1.1473	1.98

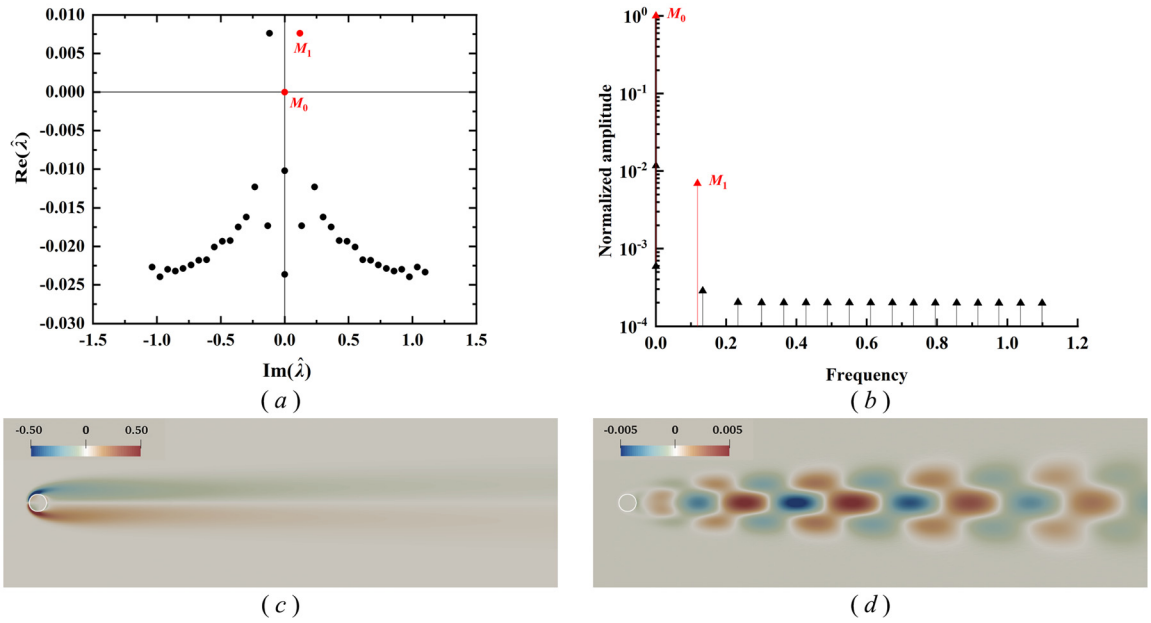

FIG. 28. Results of DMD analysis on transient cylinder-wake: (a) DMD eigenvalues in complex plane; (b) spectrum of DMD modes; (c) vorticity contours of mode M_0; and (d) vorticity contours of mode M_1 (real part).

To validate the DMD code, we perform DMD analysis on transient cylinder wake at $Re = 60$. The flow-field data are generated by conducting numerical simulation using the in-house flow solver. To prepare the data for DMD analysis, a time interval with the span of 16.91 (dimensionless time unit) is selected by using the method described in Sec. V C. (Here, the dimensionless time is defined by the free-stream velocity and diameter of the cylinder.) With a uniform sampling increment of 0.455, the total number of snapshots is 38. The DMD results are shown in Fig. 28. The distribution of eigenvalues, energy spectrum, and vorticity contours for the neutrally stable and unstable modes is in agreement with the results from Ref. 53. The predicted Strouhal numbers of the unsteady mode (i.e., mode M_1) are 0.118 and 0.125, from the present test and the reference, respectively. These two values are reasonably close to each other. The small discrepancy can be attributed to different DNS data used in performing DMD.

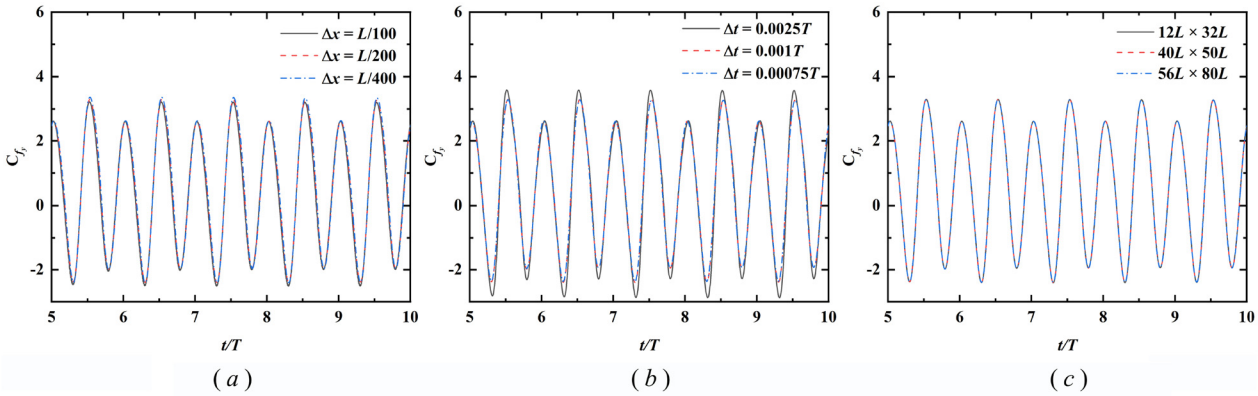

FIG. 29. Results of the mesh independence and domain independence tests: (a) The time histories of vertical force coefficient obtained by using three different mesh resolutions. The solid line, dashed line, and dashed-dotted line denote the results obtained with the grid width of $\Delta x = L/100$, $\Delta x = L/200$, and $\Delta x = L/400$, respectively. (b) The time histories of vertical force coefficient obtained by using three different time step sizes. The solid line, dashed line, and dashed-dotted line denote the results obtained by using the time step sizes of $\Delta t = 0.0025T$, $\Delta t = 0.001T$, and $\Delta t = 0.00075T$, respectively. (c) The time histories of vertical force coefficient obtained by using three different domains. The solid line, dashed line, and dashed-dotted line denote the results obtained by using the computational domains of $[12L \times 32L]$, $[40L \times 50L]$, and $[56L \times 80L]$, respectively.

TABLE II. Effect of mesh resolution on the modulus of Floquet multiplier for case ($g = 1.0$, $Re = 87.5$).

Floquet multiplier magnitude	$\Delta x = L/100$	$\Delta x = L/200$	$\Delta x = L/400$
$\lvert\mu\rvert$	1.1524	1.2025	1.2250

TABLE III. Effect of domain size on the modulus of Floquet multiplier for case ($g = 1.0$, $Re = 87.5$).

Floquet multiplier magnitude	$[12L \times 32L]$	$[40L \times 50L]$	$[56L \times 80L]$
$\lvert\mu\rvert$	1.2077	1.2025	1.2019

APPENDIX B: MESH, TIME STEP, AND DOMAIN INDEPENDENCE TESTS

To ensure that the mesh resolution used in the simulation is sufficient for obtaining accurate results, a mesh convergence test is performed. A multi-block Cartesian mesh is used in the mesh convergence test (see Fig. 2). The control parameters for the test are: $g = 1.0$, $Re = 87.5$, $\hat{L} = 0.2$, $\theta_0 = 0$, $A_\theta = \pi/12$. Three different mesh resolutions are tested, which the finest grids near the foils being $L/100$, $L/200$, and $L/400$ in spacing, respectively.

Figure 29(a) shows the time histories of vertical force coefficient, which are obtained by using three different mesh resolutions. It is clearly seen that the results are almost identical. The effect of mesh resolution on the modulus of Floquet multiplier for this case is demonstrated in Table II. It is seen that the discrepancy between the results obtained with $\Delta x = L/200$ and $\Delta x = L/400$ is sufficiently small (less than 2%).

It should be noted that $\Delta t = 0.001T$ is fixed in the tests above. The effect of the time step size on the solution is also tested. Figure 29(b) shows the time histories of vertical force coefficient obtained by using three time step sizes (the finest grid spacing is $\Delta x = L/200$ and the domain size is $[40L \times 50L]$). It can be seen that $\Delta t = 0.001T$ is sufficiently small to obtain a time step-independent solution. Furthermore, additional test also confirms that the modulus of Floquet multiplier is independent of the time step size (the result is not shown here for brevity).

A domain independence test is also conducted on the same case. The time histories of vertical force coefficient, which are obtained by using three computational domains with different sizes, are shown in Fig. 29(c). It turns out that three results are almost indistinguishable. The effect of domain size on the modulus of Floquet multiplier is also studied. As that demonstrated in Table III, the effect of domain size on the modulus is insignificant if the domain size is larger than $[40L \times 50L]$.

Based on the results of the tests above, the simulations of the present work are conducted with the mesh resolution of $\Delta x = L/200$, the time step of $\Delta t = 0.001T$, and the domain size of $[40L \times 50L]$.

REFERENCES

[1]A. Zebib, "Stability of viscous flow past a circular cylinder," J. Eng. Math. **21**, 155–165 (1987).
[2]C. P. Jackson, "A finite-element study of the onset of vortex shedding in flow past variously shaped bodies," J. Fluid Mech. **182**, 23–45 (1987).
[3]S. Kang, "Characteristics of flow over two circular cylinders in a side-by-side arrangement at low Reynolds numbers," Phys. Fluids **15**, 2486–2498 (2003).
[4]M. Carini, F. Giannetti, and F. Auteri, "First instability and structural sensitivity of the flow past two side-by-side cylinders," J. Fluid Mech. **749**, 627–648 (2014).
[5]M. Carini, F. Giannetti, and F. Auteri, "On the origin of the flip-flop instability of two side-by-side cylinder wakes," J. Fluid Mech. **742**, 552–576 (2014).
[6]C. J. Ren, L. Cheng, C. W. Xiong, F. F. Tong, and T. G. Chen, "Bistabilities in two parallel Karman wakes," J. Fluid Mech. **929**, A5 (2021).
[7]H. Honji, "Streaked flow around an oscillating circular cylinder," J. Fluid Mech. **107**, 509–520 (1981).
[8]M. Tatsuno and P. W. Bearman, "A visual study of the flow around an oscillating circular cylinder at low Keulegan–Carpenter numbers and low Stokes numbers," J. Fluid Mech. **211**, 157–182 (1990).
[9]P. Justesen, "A numerical study of oscillating flow around a circular cylinder," J. Fluid Mech. **222**, 157–196 (1991).
[10]G. Iliadis and P. Anagnostopoulos, "Viscous oscillatory flow around a circular cylinder at low Keulegan–Carpenter numbers and frequency parameters," Int. J. Numer. Methods Fluids **26**, 403–442 (1998).
[11]J. R. Elston, J. Sheridan, and H. M. Blackburn, "The transition to three-dimensionality in the flow produced by an oscillating circular cylinder," in *14th Australasian Fluid Mechanics Conference* (Adelaide University, Australia, 2001), pp. 319–322.
[12]J. R. Elston, J. Sheridan, and H. M. Blackburn, "Two-dimensional Floquet stability analysis of the flow produced by an oscillating circular cylinder in quiescent fluid," Eur. J. Mech.-B/Fluids **23**, 99–106 (2004).
[13]J. R. Elston, H. M. Blackburn, and J. Sheridan, "The primary and secondary instabilities of flow generated by an oscillating circular cylinder," J. Fluid Mech. **550**, 359–389 (2006).
[14]J. Deng and C. P. Caulfield, "Dependence on aspect ratio of symmetry breaking for oscillating foils: Implications for flapping flight," J. Fluid Mech. **787**, 16–49 (2016).
[15]D. Jallas, O. Marquet, and D. Fabre, "Linear and nonlinear perturbation analysis of the symmetry breaking in time-periodic propulsive wakes," Phys. Rev. E **95**, 063111 (2017).
[16]K. D. Jones, C. M. Dohring, and M. F. Platzer, "Experimental and computational investigation of the Knoller–Betz effect," AIAA J. **36**, 1240–1246 (1998).
[17]R. Godoy-Diana, J. L. Aider, and J. E. Wesfreid, "Transitions in the wake of a flapping foil," Phys. Rev. E **77**, 016308 (2008).
[18]C. Bose and S. Sarkar, "Investigating chaotic wake dynamics past a flapping airfoil and the role of vortex interactions behind the chaotic transition," Phys. Fluids **30**, 041701 (2018).
[19]D. Majumdar, C. Bose, and S. Sarkar, "Capturing the dynamical transitions in the flow-field of a flapping foil using immersed boundary method," J. Fluids Struct. **95**, 102999 (2020).
[20]C. Bose, S. Gupta, and S. Sarkar, "Dynamic interlinking between near-and far-field wakes behind a pitching-heaving airfoil," J. Fluid Mech. **911**, A31 (2021).
[21]S. Y. Shinde and J. H. Arakeri, "Jet meandering by a foil pitching in quiescent fluid," Phys. Fluids **25**, 041701 (2013).
[22]C. Marais, B. Thiria, J. E. Wesfreid, and R. Godoy-Diana, "Stabilizing effect of flexibility in the wake of a flapping foil," J. Fluid Mech. **710**, 659–669 (2012).
[23]X. J. Zhu, G. W. He, and X. Zhang, "How flexibility affects the wake symmetry properties of a self-propelled plunging foil," J. Fluid Mech. **751**, 164–183 (2014).
[24]S. Y. Shinde and J. H. Arakeri, "Flexibility in flapping foil suppresses meandering of induced jet in absence of free stream," J. Fluid Mech. **757**, 231–250 (2014).
[25]C. L. Shah, D. Majumdar, C. Bose, and S. Sarkar, "Chordwise flexible aft-tail suppresses jet-switching by reinstating wake periodicity in a flapping foil," J. Fluid Mech. **946**, A12 (2022).
[26]I. Ashraf, R. Godoy-Diana, J. Halloy, B. Collignon, and B. Thiria, "Synchronization and collective swimming patterns in fish (*hemigrammus bleheri*)," J. R. Soc., Interface **13**, 20160734 (2016).
[27]D. Kim, F. Hussain, and M. Gharib, "Vortex dynamics of clapping plates," J. Fluid Mech. **714**, 5–23 (2013).

[28]N. Martin, C. Roh, S. Idrees, and M. Gharib, "To flap or not to flap: Comparison between flapping and clapping propulsions," J. Fluid Mech. **822**, R5 (2017).
[29]L. A. Miller and C. S. Peskin, "A computational fluid dynamics of "clap and fling" in the smallest insects," J. Exp. Biol. **208**, 195–212 (2005).
[30]P. A. Dewey, B. M. Quinn, D. B. Boschitsch, and A. J. Smits, "Propulsive performance of unsteady tandem hydrofoils in a side-by-side configuration," Phys. Fluids **26**, 041903 (2014).
[31]Y. Bao, D. Zhou, J. J. Tao, Z. Peng, H. B. Zhu, Z. L. Sun, and H. L. Tong, "Dynamic interference of two anti-phase flapping foils in side-by-side arrangement in an incompressible flow," Phys. Fluids **29**, 033601 (2017).
[32]A. Gungor and A. Hemmati, "Wake symmetry impacts the performance of tandem hydrofoils during in-phase and out-of-phase oscillations differently," Phys. Rev. E **102**, 043104 (2020).
[33]A. Gungor, M. S. U. Khalid, and A. Hemmati, "How does switching synchronization of pitching parallel foils from out-of-phase to in-phase change their wake dynamics?," Phys. Fluids **33**, 081901 (2021).
[34]A. Gungor and A. Hemmati, "Implications of changing synchronization in propulsive performance of side-by-side pitching foils," Bioinspiration Biomimetics **16**, 036006 (2021).
[35]A. Gungor, M. S. U. Khalid, and A. Hemmati, "Classification of vortex patterns of oscillating foils in side-by-side configurations," J. Fluid Mech. **951**, A37 (2022).
[36]K. M. Raj and V. Arumurua, "Jet deflection by two side-by-side arranged hydrofoils pitching in a quiescent fluid," AIP Adv. **10**, 105128 (2020).
[37]X. Zhang, G. W. He, S. Z. Wang, and X. Zhang, "Locomotion of a bioinspired flyer powered by one pair of pitching foils," Phys. Rev. Fluids **3**, 013102 (2018).
[38]Y. Liu, C. Pan, and Y. P. Liu, "Propulsive performance and flow-field characteristics of a jellyfish-like ornithopter with asymmetric pitching motion," Phys. Fluids **32**, 071904 (2020).
[39]X. Zhang, G. W. He, S. Z. Wang, and X. Zhang, "Passive hovering of a flexible Λ-flyer in a vertically oscillating airflow," J. Fluid Mech. **878**, 113–146 (2019).
[40]D. B. Quinn, K. W. Moored, P. A. Dewey, and A. J. Smits, "Unsteady propulsion near a solid boundary," J. Fluid Mech. **742**, 152–170 (2014).
[41]D. B. Quinn, G. V. Lauder, and A. J. Smits, "Flexible propulsors in ground effect," Bioinspiration Biomimetics **9**, 036008 (2014).
[42]A. Mivehchi, J. Dahl, and S. Licht, "Heaving and pitching oscillating foil propulsion in ground effect," J. Fluids Struct. **63**, 174–187 (2016).
[43]M. Kurt, J. Cochran-Carney, Q. Zhong, A. Mivehchi, D. B. Quinn, and K. M. Moored, "Swimming freely near the ground leads to flow-mediated equilibrium altitudes," J. Fluid Mech. **875**, R1 (2019).
[44]Q. Zhong, T. J. Han, K. W. Moored, and D. B. Quinn, "Aspect ratio affects the equilibrium altitude of near-ground swimmers," J. Fluid Mech. **917**, A36 (2021).
[45]G. Floquet, "Sur les équations différentielles linéaires á coefficients périodiques," Ann. Sci. École Norm. Super. **12**, 47–88 (1883).
[46]S. Z. Wang and X. Zhang, "An immersed boundary method based on discrete stream function formulation for two- and three-dimensional incompressible flows," J. Comput. Phys. **230**, 3479–3499 (2011).
[47]X. J. Zhu, G. W. He, and X. Zhang, "An improved direct-forcing immersed boundary method for fluid-structure interaction simulations," J. Fluids Eng. **136**, 040903 (2014).
[48]S. Z. Wang, G. W. He, and X. Zhang, "Parallel computing strategy for a flow solver based on immersed boundary method and discrete stream-function formulation," Comput. Fluids **88**, 210–224 (2013).
[49]L. S. Tuckerman and D. Barkley, "Bifurcation analysis for timesteppers," in *Numerical Methods for Bifurcation Problems and Large-Scale Dynamical Systems*, edited by E. Doedel and L. S. Tuckerman (Springer, New York, 2000), pp. 453–466.
[50]Y. Saad, *Numerical Methods for Large Eigenvalue Problems* (Society for Industrial and Applied Mathematics, Philadelphia, 2011).
[51]N. Demo, M. Tezzele, and G. Rozza, "PyDMD: Python dynamic mode decomposition," J. Open Source Software **3**, 530 (2018).
[52]J. H. Tu, C. W. Rowley, D. M. Luchtenburg, S. L. Brunton, and J. N. Kutz, "On dynamic mode decomposition: Theory and applications," J. Comput. Dny. **1**, 391–421 (2014).
[53]K. K. Chen, J. H. Tu, and C. W. Rowley, "Variants of dynamic mode decomposition: Boundary condition, Koopman, and Fourier analyses," J. Nonlinear Sci. **22**, 887–915 (2012).
[54]T. Weis-Fogh, "Energetics of hovering flight in hummingbirds and in drosophila," J. Exp. Biol. **56**, 79–104 (1972).
[55]T. Weis-Fogh, "Quick estimates of flight fitness in hovering animals, including novel mechanisms for lift production," J. Exp. Biol. **59**, 169–230 (1973).
[56]J. Higgins III, M. Ford, and J. Costello, "Transitions in morphology, nematocyst distribution, fluid motions, and prey capture during development of the scyphomedusa *Cyanea capillata*," Biol. Bull. **214**, 29–41 (2008).
[57]S. Teneda, "Downstream development of the wakes behind cylinders," J. Phys. Soc. Jpn. **14**, 843–848 (1959).
[58]T. Matsui and M. Okude, "Formation of the secondary vortex street in the wake of a circular cylinder," in *Structure of Complex Turbulent Shear Flow*, edited by R. Dumas and L. Fulachier (Springer, Berlin, 1983), pp. 156–164.
[59]C. H. K. Williamson and A. Prasad, "A new mechanism for oblique wave resonance in the 'natural' far wake," J. Fluid Mech. **256**, 269–313 (1993).
[60]J. M. Cimbala, H. M. Nagib, and A. Roshko, "Large structure in the far wakes of two-dimensional bluff bodies," J. Fluid Mech. **190**, 265–298 (1988).
[61]B. Kumar and S. Mittal, "On the origin of the secondary vortex street," J. Fluid Mech. **711**, 641–666 (2012).
[62]O. Inoue and T. Yamazaki, "Secondary vortex streets in two-dimensional cylinder wakes," Fluid Dyn. Res. **25**, 1–18 (1999).
[63]H. Y. Jiang, "Formation mechanism of a secondary vortex street in a cylinder wake," J. Fluid Mech. **915**, A127 (2021).
[64]L. Shaabani-Ardali, D. Sipp, and L. Lesshafft, "Vortex pairing in jets as a global Floquet instability: Modal and transient dynamics," J. Fluid Mech. **862**, 951–989 (2019).
[65]M. Carini, F. Auteri, and F. Giannetti, "Secondary instabilities of the in-phase synchronized wakes past two circular cylinders in side-by-side arrangement," J. Fluids Struct. **53**, 70–83 (2015).
[66]S. Bagheri, "Koopman-mode decomposition of the cylinder wake," J. Fluid Mech. **726**, 596–623 (2013).